catalysts

MDPI

Article

# Aqueous and Surface Chemistries of Photocatalytic Fe-Doped $CeO_2$ Nanoparticles

**Duangdao Channei [1,2], Sukon Phanichphant [3,*], Auppatham Nakaruk [4,5,*], Sajjad S. Mofarah [6], Pramod Koshy [6] and Charles C. Sorrell [6]**

1 Department of Chemistry, Faculty of Science, Naresuan University, Phitsanulok 65000, Thailand; duangdaoc@nu.ac.th
2 Research Center for Academic Excellence in Petroleum, Petrochemicals and Advanced Materials, Naresuan University, Phitsanulok 65000, Thailand
3 Materials Science Research Center, Faculty of Science, Chiang Mai University, Chiang Mai 50200, Thailand
4 Department of Industrial Engineering, Faculty of Engineering, Naresuan University, Phitsanulok 65000, Thailand
5 Centre of Excellence for Innovation and Technology for Water Treatment, Naresuan University, Phitsanulok 65000, Thailand
6 School of Materials Science and Engineering, Faculty of Science, UNSW Sydney, Sydney, NSW 2052, Australia; s.seifimofarah@student.unsw.edu.au (S.S.M.); koshy@unsw.edu.au (P.K.); c.sorrell@unsw.edu.au (C.C.S.)
* Correspondence: sphanichphant@yahoo.com (S.P.); auppathamn@nu.ac.th (A.N.); Tel.: +66-53-943-345 (S.P.); +66-87-362-0558 (A.N.); Fax: +66-53-892-277 (S.P.); +66-55-961-103 (A.N.)

Academic Editors: Enrique Rodríguez-Castellón, Agustín Bueno-López and Elisa Moretti
Received: 7 November 2016; Accepted: 23 January 2017; Published: 29 January 2017

**Abstract:** The present work describes the effects of water on Fe-doped nanoparticulate $CeO_2$, produced by flame spray pyrolysis, which represent a critical environmental issue because $CeO_2$ is not stable in typical atmospheric conditions. It is hygroscopic and absorbs ~29 wt % water in the bulk when exposed to water vapor but, more importantly, it forms a hydrated and passivating surface layer when immersed in liquid water. In the latter case, $CeO_2$ initially undergoes direct and/or reductive dissolution, followed by the establishment of a passivating layer calculated to consist of ~69 mol % solid $CeO_2{\cdot}2H_2O$ and ~30 mol % gelled $Ce(OH)_4$. Under static flow conditions, a saturated boundary layer also forms but, under turbulent flow conditions, this is removed. While the passivating hydrated surface layer, which is coherent probably owing to the continuous $Ce(OH)_4$ gel, would be expected to eliminate the photoactivity, this does not occur. This apparent anomaly is explained by the calculation of (a) the thermodynamic stability diagrams for Ce and Fe; (b) the speciation diagrams for the $Ce^{4+}$-$H_2O$, $Ce^{3+}$-$H_2O$, $Fe^{3+}$-$H_2O$, and $Fe^{2+}$-$H_2O$ systems; and (c) the Pourbaix diagrams for the Ce-$H_2O$ and Fe-$H_2O$ systems. Furthermore, consideration of the probable effects of the localized chemical and redox equilibria owing to the establishment of a very low pH (<0) at the liquid-solid interface also is important to the interpretation of the phenomena. These factors highlight the critical importance of the establishment of the passivating surface layer and its role in photocatalysis. A model for the mechanism of photocatalysis by the $CeO_2$ component of the hydrated phase $CeO_2{\cdot}2H_2O$ is proposed, explaining the observation of the retention of photocatalysis following the apparent alteration of the surface of $CeO_2$ upon hydration. The model involves the generation of charge carriers at the outer surface of the hydrated surface layer, followed by the formation of radicals, which decompose organic species that have diffused through the boundary layer, if present.

**Keywords:** cerium oxide; nanoparticles; photocatalysis; aqueous chemistry; surface chemistry; thermodynamic stability diagrams; speciation diagrams; Pourbaix diagrams

## 1. Introduction

Ceria ($CeO_2$) is well known as a photocatalyst and Fe doping of $CeO_2$ improves its photocatalytic performance [1–4]. However, it is less well known that, in common with many rare earth oxides [5,6], $CeO_2$ is hygroscopic and hence water can be absorbed upon exposure to atmospheric water vapor. A second potential outcome of this water absorption is the conversion from the oxide to a hydrated and/or hydroxylated phase at the surface [7], particularly upon exposure to liquid water. The present work shows that nanoparticulate $CeO_2$ (~6 nm) exhibits weight gains from the absorption of water vapor in the range ~29–34 wt % when doped with 0–2 mol % Fe (metal basis), respectively. Despite the associated alteration of the $CeO_2$ bulk and surface, where photocatalysis takes place, the presence of a potentially coherent hydrated and/or hydroxylated phase on the surface allows the maintenance of the photocatalytic activity. The present work, which follows previous work on the fabrication, analyses, and photocatalytic performance of Fe-doped $CeO_2$ nanopowders [8], considers the nature of this surface layer when $CeO_2$ is immersed in liquid water and the soluble species associated with it.

Redox equilibria ($Ce^{4+} \leftrightarrow Ce^{3+}$) for pure $CeO_2$ generally are considered generically in terms of Equation (1):

$$2CeO_2\ (s) = Ce_2O_3\ (s) + {}^1/_2O_2(g) \quad (1)$$

However, the Ce-O phase diagram [9] shows that $CeO_2$ exhibits a large solid solution homogeneity region and that $Ce_2O_3$ is a separate compound. Consequently, it is more appropriate to consider $CeO_2$ in light of the oxygen vacancies associated with its nonstoichiometry [10–12], so $CeO_2$ is expressed more accurately in different forms as given in Equation (2):

$$CeO_2\ (s) = CeO_{2-x}\ (s) = Ce^{4+}_{1-x}Ce^{3+}_xO^{2-}_{2-0.5x}\ (s) = Ce^{4+}_{1-x}Ce^{3+}_xO^{2-}_{2-0.5x}\square_x\ (s) \quad (2)$$

where:

$\square$ = oxygen vacancy ($V_O^{\bullet\bullet}$)

Since the presence of oxygen vacancies is known to be associated with water absorption and hygroscopicity [7,13], then it is probable that the extent of nonstoichiometry ($x$) is proportional to the degree of hygroscopicity.

The influence of iron doping ($Ce_{1-y}Fe_yO_{2-x}$) on the generation of oxygen vacancies conventionally is illustrated by the Kröger-Vink [14] notation for the defect equilibria, which are given in Equations (3) and (4):

Ionic compensation:

$$Fe_2O_3\ (s) \overset{CeO_2}{\leftrightarrow} 2Fe'_{Ce} + V_O^{\bullet\bullet} + 3O^x_O \quad (3)$$

Electronic compensation:

$$Fe_2O_3(s) + {}^1/_2O_2(g) \overset{CeO_2}{\leftrightarrow} 2Fe'_{Ce} + 2h^{\bullet} + 4O^x_O \quad (4)$$

where:

$Fe'_{Ce}$ = $Fe^{3+}$ substituting on the $Ce^{4+}$ site (single net negative charge)
$O^x_O$ = Oxygen on the oxygen site (no charge)
$V_O^{\bullet\bullet}$ = Oxygen vacancy (double net positive charge)
$h^{\bullet}$ = Electron hole (single net positive charge)

It can be assumed that $Fe^{3+}$ substitutes on the $Ce^{4+}$ lattice site in $CeO_2$, which crystallizes in the fluorite structure [15], because the progressively hygroscopic behavior is attributed to the progressive generation of oxygen vacancies with increasing Fe doping level, as discussed subsequently. However, the eightfold ionic radii of $Fe^{3+}$ (0.092 nm [16]) and $Ce^{4+}$ (0.111 nm [16]) differ by 17%, which suggests that only limited solubility would be expected [17].

$CeO_2$ is a wide-band-gap semiconductor with an optical indirect band gap of 3.20 eV [18]. The first part of this sequence of publications [8] showed that Fe doping progressively lowered the band gap

from 3.18 eV for undoped $CeO_2$ to 2.90 eV for $CeO_2$ doped with 2 mol % Fe (metal basis). The present work demonstrates that the Fe doping increased the hygroscopicity and hence the degree of hydration, with the associated alteration of both the bulk and surface. At the same time, the photocatalytic performance increased with increasing doping level [8]. The apparent contradiction that is derived from the simultaneous improvement in performance and alteration of the surface is considered in the present work by examining the ionic and polynuclear species likely to be present in the hydrated surface layer.

Consequently, the objectives of the present work were to examine: (a) how the surfaces of $CeO_2$ and $CeO_2$ doped with Fe are altered upon exposure to water over a range of pH; (b) the possible ionic and polynuclear species that are thermodynamically able to form upon hydration; and (c) their concentrations in the surrounding solution. These goals were achieved through the generation of the following for Ce- and Fe-containing species:

- Thermodynamic stability diagrams
- Speciation diagrams
- Pourbaix diagrams

The generation of these diagrams clarified the nature of the alteration of both undoped $CeO_2$ and Fe-doped $CeO_2$ during processing by flame spray pyrolysis [8] and, in the present work, upon hydration resulting from exposure to 100% relative humidity.

## 2. Experimental Procedure and Results

### *2.1. Water Absorption*

The differences between the nominal amounts of dopant added (0–2 mol % metal basis) and those present in the synthesized particles were assessed using energy dispersive X-ray spectroscopy (EDS, JEOL JSM-6335F, 15 kV accelerating voltage, JEOL, Tokyo, Japan).

The undoped $CeO_2$ and Fe-doped $CeO_2$ fabricated by flame spray pyrolysis [8] were examined for water absorption (and adsorption) by weighing hydrated and desiccated nanopowders using a digital balance with 0.0001 g precision. Hydration was performed by placing ~0.15 g of nanopowder in a plastic bag containing a non-contacting water-saturated sponge and sealing the bag, which subjected the nanopowders to 100% relative humidity (RH) for 48 h. Desiccation was performed by subsequent heating at 120 °C for 2 h, which was determined by repeat measurements to be sufficient for complete drying. The weight difference reflected the extent of the absorption of water vapor.

The effects of water vapor absorption on the crystal lattice following absorption and dessication were determined by X-ray diffraction (XRD, Philips X'pert Multi-Purpose Diffractometer, CuKα radiation, 45 kV, 40 mA, step size 0.02° 2θ, scanning speed 5.5° 2θ/min, aluminum sample holder, Philips, Amsterdam, Netherlands). The relative positions of the (111) plane spacing (28.59° 2θ) of $CeO_2$, which is the major peak in the XRD pattern, were assessed as a function of the Fe dopant level using the major $d_{(104)}$ peak (29.35° 2θ) of $CaCO_3$ as a normalizing internal standard (35 wt %). The crystallite sizes were calculated using the Scherrer equation [19] for the same $CeO_2$ $d_{(111)}$ peak of the XRD patterns and a shape factor of 0.9.

The particle sizes were estimated in terms of the Sauter mean diameter (SMD) [20] using the specific surface area (SSA), which was determined using the Brunauer, Emmett, and Teller (BET) nitrogen adsorption method (Quantachrome Autosorp 1 MP, 0.25 g sample, 1 h at 150 °C degassing) [21], assuming a true density of $CeO_2$ of 7216 kg/m$^3$ [22]. The particle sizes were confirmed qualitatively by the inspection of images obtained by high-resolution transmission electron microscopy (HRTEM, JEOL JEM-2010, 200 kV accelerating voltage).

Water absorption/adsorption by $CeO_2$ is initiated in water at the liquid-solid interface or in humid air at the gas-solid interface. When exposed to water, this solid surface has been shown to reduce from $Ce^{4+}$ ($CeO_2$) to $Ce^{3+}$ ($CeO_{2-x}$) [23–25], with the consequent formation of oxygen vacancies [26–31]. The adsorption location is normally on the (111) plane [32], where the reduction occurs according to Equation (1) or, in ionic terms:

$$2Ce_{Ce}^{x} + 4O_{O}^{x} \overset{Ce_2O_3}{\leftrightarrow} 2Ce'_{Ce} + V_{O}^{\bullet\bullet} + 3O_{O}^{x} + O_2\ (g) \quad (5)$$

where:

$Ce_{Ce}^{x}$ = $Ce^{4+}$ on the $Ce^{4+}$ site (no charge)
$Ce'_{Ce}$ = $Ce^{3+}$ on the $Ce^{4+}$ site (single net negative charge)
$O_{O}^{x}$ = Oxygen on the oxygen site (no charge)
$V_{O}^{\bullet\bullet}$ = Oxygen vacancy (double net positive charge)

The results for the preceding characterisation procedures are given in Table 1. These data demonstrate that (a) $CeO_2$ is strongly hygroscopic and (b) Fe doping has a significant influence on increasing the hygroscopicity. This is not surprising since the expected oxidation state of $Fe^{3+}$ also should enhance oxygen vacancy formation according to Equation (3), assuming that $Fe^{3+}$ (crystal radius$^{VIII}$ = 0.092 nm [16]) substitutes for $Ce^{4+}$ (crystal radius$^{VIII}$ = 0.111 nm [16]). Although the mismatch is ~17%, which is slightly higher than that suggested for extensive solid solubility (15%) [17], the formation of $Ce_yFe_{1-y}O_{2-x}$ solid solution has been reported previously [33,34]. However, the substitution of $Ce^{3+}$ by $Fe^{3+}$ is much less likely owing to the large size of the former (crystal radius$^{VIII}$ = 0.1283 nm [16]) and the associated ~28% mismatch. Hence, the $Ce_yFe_{1-y}O_{2-x}$ solid solution can be considered more likely to result in oxygen deficiency and potentially could lead to oxygen vacancy formation (in the generally assumed case of ionic compensation).

**Table 1.** Effects of the absorption of water vapor on Fe-doped $CeO_2$.

| Parameter | | Unit | Fe Dopant Concentration (mol % Metal Basis) * | | | | | Reference |
|---|---|---|---|---|---|---|---|---|
| | | | **0** | **0.36** | **0.96** | **1.38** | **1.73** | |
| Absorbed Water | | wt % | 28.6 | 30.6 | 31.3 | 32.3 | 34.1 | Present Work |
| $d_{(111)}$ Spacing | Before Heating | nm | 0.3150 | 0.3138 | 0.3131 | 0.3124 | 0.3122 | |
| | After Heating | nm | 0.3141 | 0.3137 | 0.3129 | 0.3126 | 0.3115 | |
| Crystallite Size | | nm | 7.15 | 6.65 | 6.41 | 6.31 | 6.22 | [8] |
| Particle Size | | nm | 6.40 | 6.16 | 6.03 | 5.98 | 5.94 | |
| Specific Surface Area | | $m^2/g$ | 130 | 135 | 138 | 139 | 140 | |

* The five Fe dopant concentrations above were determined by EDS to correspond to the five nominal Fe dopant concentrations of 0, 0.50, 1.00, 1.50, and 2.00 mol % Fe (metal basis), respectively [8].

Figure 1 shows a representative agglomerated nanostructure, in which it can be seen that the typical particle size of ~6 nm (Table 1), which was calculated assuming a spherical shape [20], corresponds reasonably well to the equiaxed $CeO_2$ octahedra in the size range of 2–7 nm.

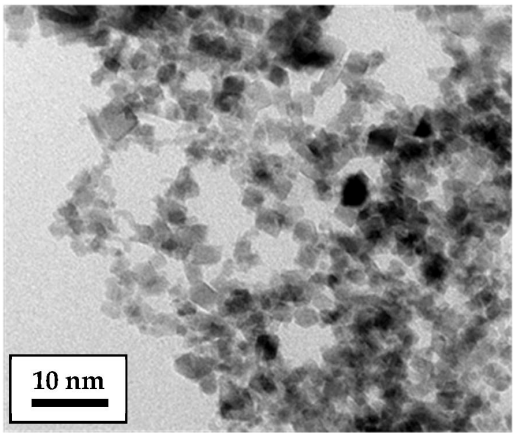


**Figure 1.** Representative agglomerated nanostructure of $CeO_2$ doped with 1.00 mol % Fe (metal basis) fabricated by flame spray pyrolysis (FSP) at >1300 °C and log $p(O_2)$ = −0.15.

The $d_{(111)}$ data in Table 1 show that the volume hydration caused lattice spacing contraction. On one hand, lattice expansion would be expected owing to the additional volume occupied by the water groups, thereby forming $CeO_2 \cdot 2H_2O$, or hydroxyl groups, thereby forming $Ce(OH)_4$. On the other hand, lattice contraction would be expected owing to the substitution by the smaller $Fe^{3+}$ relative to $Ce^{4+}$ ($Ce^{3+} \leftrightarrow Fe^{3+}$ substitution is unlikely) as well as the associated formation of oxygen vacancies (assuming ionic compensation). These data clearly support the latter mechanisms. The lack of linearity of the data probably is indicative of (a) concentration gradients through the bulk of the solid and/or (b) the variation in the structural defectiveness of the $Ce_yFe_{1-y}O_{2-x}$ solid solution. Nonetheless, the trends in lattice spacing and structural modification are clear.

### *2.2. Thermodynamic Stability Diagrams*

Thermodynamic stability diagrams show different regions of existence of ions of different valences (and hence the corresponding oxides) as a function of temperature and pressure. Consequently, these diagrams are useful in estimating the potential valence states and mixtures of valences present under the relevant experimental conditions. In the present work, FactSage 6.2 software (Predom mode, which is used to calculate stability diagrams) and the associated database [35] were used to calculate and plot the valences present as a function of temperature and oxygen partial pressure ($pO_2$). Calculations for each temperature were done individually over a range of values of interest, yielding plots of stability regions that are indicative of the dominant valence or valences, e.g., $Ce^{4+}$ for $CeO_2$, $Ce^{3+}$ for $Ce_2O_3$, etc.

Figures 2 and 3 show the respective thermodynamic stability diagrams for Ce ($Ce_aO_b$) and Fe ($Fe_aO_b$) for the temperature range 0 °C to 1700 °C and log $pO_2$ range −30 to 0 (based on atm). The experimental conditions [4] during flame spray pyrolysis (FSP) of >1300 °C and log $pO_2 = -0.15$ can be visualized in the diagrams so that the prevailing conditions during processing and subsequently upon cooling can be estimated. These data show that processing and cooling to room temperature should yield the dominant oxides $CeO_2$ ($Ce^{4+}$) and $Fe_2O_3$ ($Fe^{3+}$). However, owing to temperature uncertainty and variability, $Fe_3O_4$ ($Fe^{2+}/Fe^{3+}$ or $FeO \cdot Fe_2O_3$) may have formed and been retained during quenching [36]. These diagrams also provide guidance for alternative processing protocols, where lower $pO_2$ can result in different valences during high-temperature processing and, upon cooling through other stability regions, can yield multivalent mixtures.

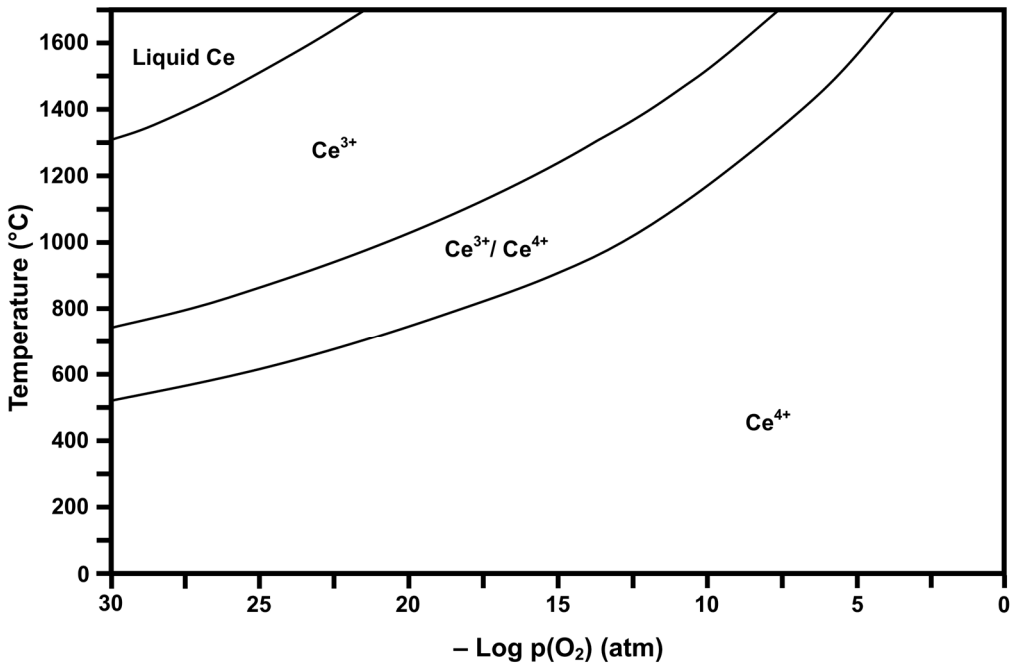


**Figure 2.** Calculated Ce stability diagram ($Ce^{4+} = CeO_2$, $Ce^{3+}/Ce^{4+} = Ce_3O_5$ or $CeO_2 \cdot Ce_2O_3$, $Ce^{3+} = Ce_2O_3$).

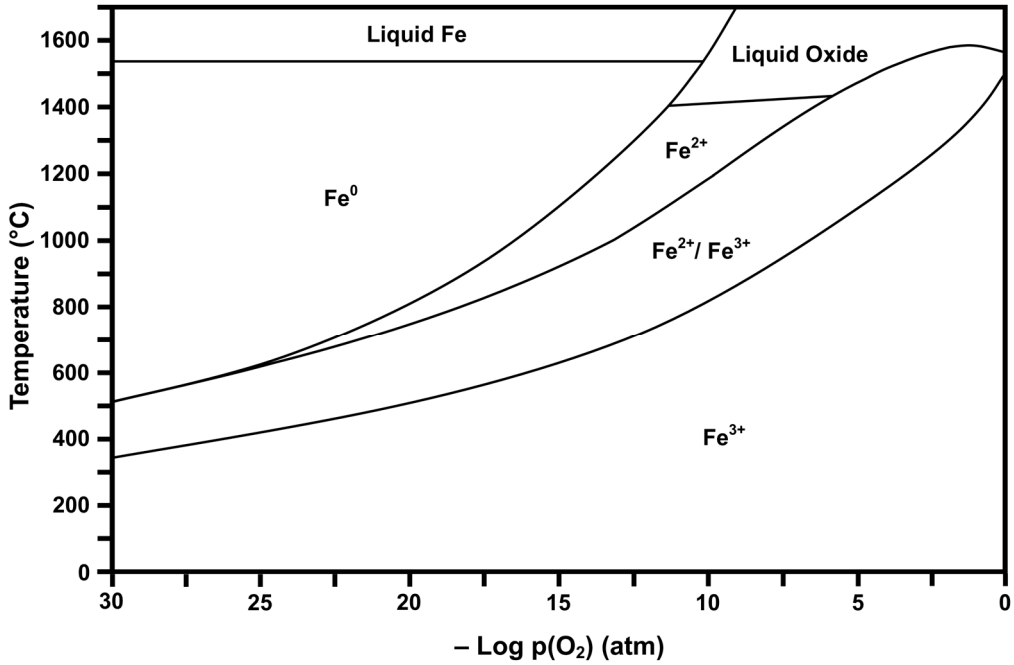


**Figure 3.** Calculated Fe stability diagram ($Fe^{3+}$ = $Fe_2O_3$, $Fe^{2+}/Fe^{3+}$ = $Fe_3O_4$ or $FeO{\cdot}Fe_2O_3$, $Fe^{2+}$ = FeO, $Fe^0$ = elemental Fe).

### 2.3. Speciation Diagrams

While the thermodynamic stability diagrams indicate the most probable oxide species present during and after processing, they do not indicate the response of these oxides to water exposure. Speciation diagrams allow tentative assessment of the types and concentrations of the species that can form upon hydration, solution formation, and precipitation.

However, while speciation data indicate the species in the surrounding aqueous solution under equilibrium conditions, the equilibria between the solution and the solid interface are mediated by the kinetics governing the potential establishment of a dense passivating hydrated and/or hydroxylated surface layer as well as a boundary layer of solution saturated with species derived from the hydrated surface layer [28,37,38].

The formation of the aqueous species is based on the respective equilibrium constants ($K^0$), which are effectively the hydrolysis constants ($K_h$) for these aqueous systems. The $K_h$ then are used to calculate the speciation diagram of each ion and polycomplex of specific valence [39] under standard state conditions of 298 K and 1 atm air. The concentrations of both cerium and iron species were set at 10 μM as this is a commonly used value that gives an upper limit to the typical range of dilute solutions ($10^{-10}$–$10^{-6}$ M [40]). The diagrams are plotted in terms of the logarithms of the concentrations of the ionic and polynuclear species as a function of the pH of the solution. The scale of the solute concentrations is notable as it can be so low as to be insignificant; some speciation diagrams do not indicate the polynuclear species and so the scale is truncated above the relevant concentrations. The van't Hoff equation is used to determine the $K_h$ values from the relevant thermodynamic data in the form of Gibbs standard free energies of reaction ($\Delta G_r^0$), as shown in Equation (6) [41]:

$$\Delta G_r^0 = -RT \ln K_h \quad (6)$$

where:

$\Delta G_r^0$ = Gibbs standard free energy of reaction (J/mol)
R = Gas constant (8.314 J/K·mol)
$T$ = Absolute temperature (K)
$K_h$ = Hydrolysis constant

The speciation diagrams calculated for the aqueous systems are shown in Figures 4–7. These diagrams were constructed using the software MEDUSA (Make Equilibrium Diagrams Using Sophisticated Algorithms, 32 Bit Version, Ignasi Puigdomenech, Inorganic Chemistry, Royal Institute of Technology, Stockholm, Sweden, 16 December 2010) and the associated database HYDRA (Hydrochemical Equilibrium Constant Database) [42]. However, more recent thermodynamic data also were used for these calculations and those used to generate the Pourbaix diagrams; these data are discussed subsequently. Speciation diagrams assume that there are no interactions between species and that there is absolute hydrolysis, where there is only proton transfer during the processes, not electron transfer. Consequently, at constant temperature, pressure, and initial concentration, the reactions are dependent on the pH, which is determined by the $K_h$.

The speciation diagrams for $Ce^{4+}$-$H_2O$ and $Ce^{3+}$-$H_2O$, which are shown in Figures 4 and 5, respectively, were calculated in order to harmonize with the Pourbaix diagram of Hayes et al. [43]. In many cases, Pourbaix diagrams treat solids and liquids independently (except for the elemental forms). In the present work, soluble species and some precipitates are included together in order to reflect the experimental observations for the Pourbaix diagram of Hayes et al. [43]. The intersection of two species on a speciation diagram corresponds to identical concentrations of both at a given pH (assuming equal activity coefficients).

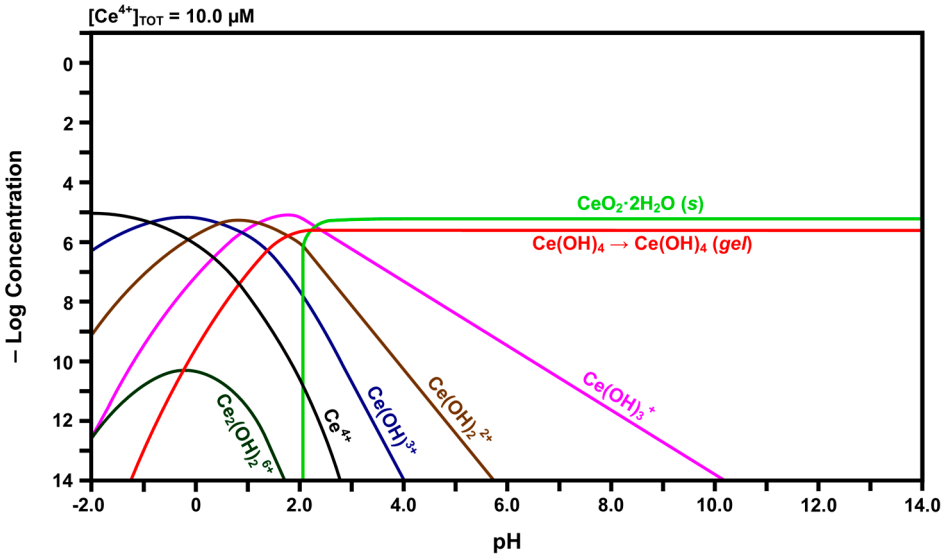


**Figure 4.** Calculated speciation diagram of $Ce^{4+}$-$H_2O$.

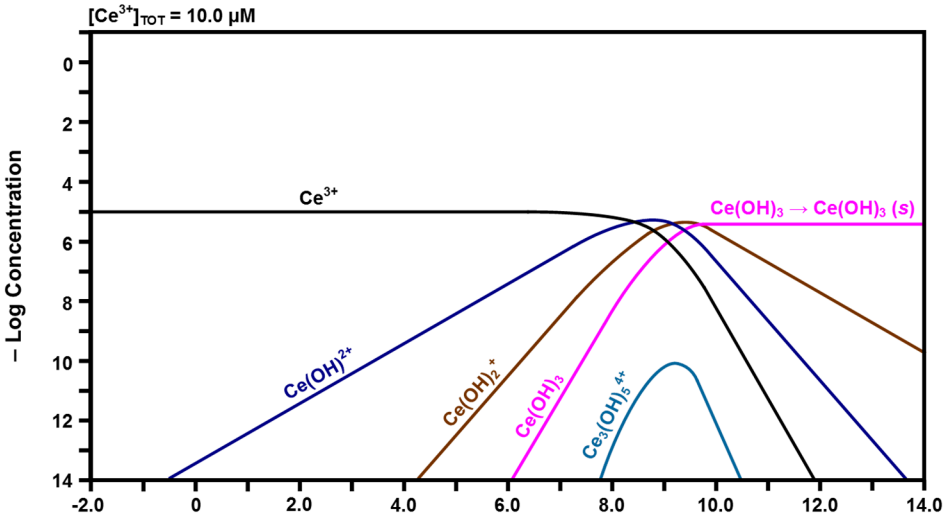


**Figure 5.** Calculated speciation diagram of $Ce^{3+}$-$H_2O$.

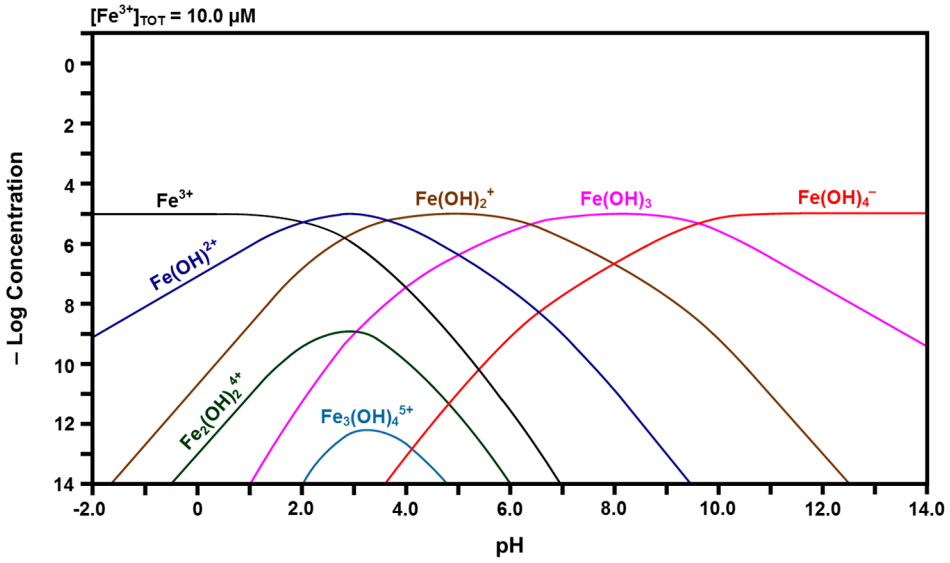


**Figure 6.** Calculated speciation diagram of $Fe^{3+}$-$H_2O$.

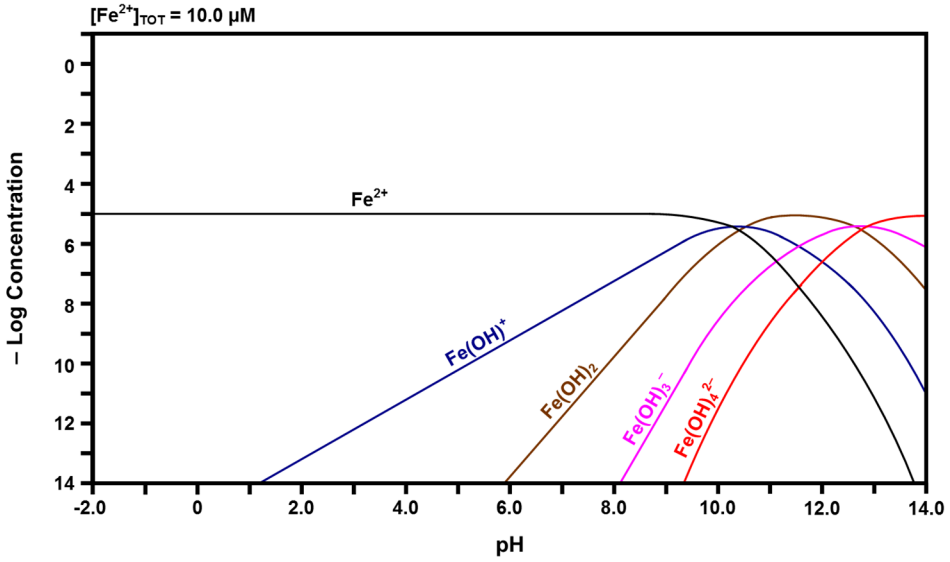


**Figure 7.** Calculated speciation diagram of $Fe^{2+}$-$H_2O$.

Inspection of the curve for $Ce^{4+}$ in Figure 4 reveals that, with increasing pH, its concentration decreases rapidly while the concentrations of the species for which there are curve intersections increase. That is, $Ce^{4+}$ hydrolyzes progressively with increasing pH to form $Ce(OH)^{3+}$, $Ce(OH)_2{}^{2+}$, $Ce(OH)_3{}^{+}$, and finally $Ce(OH)_4$. The latter species subsequently undergoes gelation [43], so this is indicated in the curve for this species. This indicates that free $Ce^{4+}$ cations are relatively unstable and readily attract hydroxyl groups. At a pH of slightly greater than 2.00, solid $CeO_2{\cdot}2H_2O$ begins to precipitate. The intersection of the three curves at a pH of ~2.60 shows that solid $CeO_2{\cdot}2H_2O$ also precipitates from $Ce(OH)_3{}^{+}$ at this point. Although $Ce(OH)_4$ also forms from $Ce(OH)_3{}^{+}$ at this point, the presence of the inflection point for the curve for $Ce(OH)_4$ at this pH suggests that this is the point at which it changes from a solute to a gel. However, the experimental observations concerning the Pourbaix diagram revealed that the equilibria were sensitive to the atmosphere. Under argon, $Ce(OH)_4$ readily precipitated with increasing pH, probably as a gel; in contrast, under air, a mixture of precipitated $CeO_2{\cdot}2H_2O$ and gelled $Ce(OH)_4$ formed with increasing pH. Thus, these two species, which are chemically identical, are included in the speciation diagram, even though they are not solutes, so that there is a direct correspondence between the speciation diagram and the experimental observations concerning the Pourbaix diagram. Finally, the speciation diagram shows that the dimerisation of two $Ce(OH)^{3+}$ species to form dinuclear $Ce_2(OH)_2{}^{6+}$ occurs at very low concentrations.

In contrast, the curve for $Ce^{3+}$ in Figure 5 shows that free $Ce^{3+}$ is more stable as a function of pH and remains the predominant species at low pH up to ~8.00. It is clear that the same progression of hydrolysis occurs for the conversion of $Ce^{3+}$ to $Ce(OH)_3$. The greater stability of $Ce^{3+}$ is attributed to the lower field strength of $Ce^{3+}$ relative to that of $Ce^{4+}$, which provides a lower driving force for hydrolysis [44], leading to the formation of $Ce(OH)^{2+}$, $Ce(OH)_2{}^{+}$, and finally $Ce(OH)_3$, although the pH range over which this occurs is smaller than for the $Ce^{4+}$ species. Furthermore, the inclusion of solid $Ce(OH)_3$ is based on similar experimental observations for the Pourbaix diagram of Hayes et al. [43], which showed that $Ce(OH)_3$ precipitated when the pH exceeded ~10.00. The data for trinuclear $Ce_3(OH)_5{}^{4+}$, which forms from $Ce(OH)^{2+}$ or $Ce(OH)^{2+}$ + $Ce(OH)_2{}^{+}$, were not available in the HYDRA database [42] but the $K_h$ was obtained from elsewhere [44]. Furthermore, data for $Ce(OH)_4{}^{-}$ are present in the database but they are inconsistent with the other data calculated in the present work. Consequently, the data for $Ce(OH)_4{}^{-}$ are subject to rejection and this is supported by the observation that this species does not form during hydrolysis [45].

The data in these speciation diagrams allow some significant inferences concerning the events that take place when $CeO_{2-x}$ is immersed in water under atmospheric conditions. Since particulate $CeO_{2-x}$ is known to exhibit oxygen vacancies at the surface [46], then it is clear that the surface contains some fraction of $Ce^{3+}$ species associated with the oxygen vacancies while the bulk volume consists predominantly of $Ce^{4+}$ species. Consequently, the surface contains both $Ce^{3+}$ and $Ce^{4+}$ species that can be leached when the solid is immersed in water.

The speciation diagram of Figure 5 suggests that the surface will be dissolved partially, initially generating the major soluble species $Ce^{3+}$ at a constant concentration. As the localized pH at the liquid-solid interface increases upon equilibration with its surrounding aqueous environment of pH ~7.00, the concentration of the second major soluble species $Ce(OH)^{2+}$ increases. The same effect occurs for $Ce(OH)_2{}^{+}$ and $Ce(OH)_3$ as the pH increases, although the concentrations of these species remain negligible. Therefore, these are the solutes that have the possibility of being present in the surrounding solution, which is at a nominal pH of ~7.00.

In contrast, the speciation diagram of Figure 4 shows that $Ce^{4+}$ also is dissolved initially but that its low stability results in a relatively rapid shift in overall composition across the range of hydroxide species as the pH at the liquid-solid interface rapidly increases owing to hydrolysis and equilibration between the solid and liquid. While the nominal pH of the surrounding solution is ~7.00, the localized pH at the liquid-solid interface is unknown but it is established through the equilibrium between water and a solid of extremely high $Ce^{3+}$ and $Ce^{4+}$ concentrations. Consequently, the localized pH must be very low, probably <0, and so the major soluble species are confirmed as being $Ce^{4+}$ and $Ce^{3+}$. The pH gradient at the interface can be visualized as being asymptotic, increasing rapidly from <0 to ~7.00 as the distance from the interface into the solution increases. When the pH reaches ~2.60, the formation of a mixture of solid $CeO_2{\cdot}2H_2O$ and gelled $Ce(OH)_4$ is facilitated, after which the concentrations of the remaining hydroxide species decrease. By pH ~7.00, the only remaining solute being generated is $Ce(OH)_3{}^{+}$ but its concentration is so low as to be negligible.

In light of the preceding data, it is clear that solid $CeO_2{\cdot}2H_2O$ and gelled $Ce(OH)_4$ formed upon the hydration of the Fe-doped nanoceria by water vapor, so these solids also formed a hydrated and/or hydroxylated surface layer on $CeO_{2-x}$. For $CeO_2$ exposed to water vapor, these phases would be present in the bulk. In contrast, for $CeO_2$ immersed in liquid water, these phases would be present only on the surface as they form a coherent passivating layer of the insoluble solids, viz., precipitated $CeO_2{\cdot}2H_2O$ and gelled $Ce(OH)_4$. Since the pH would not reach a value of ~9.75, Figure 5 shows that solid $Ce(OH)_3$ would not precipitate and become a component of the surface layer.

The aqueous solubility of solid $Ce(OH)_4$ is reported to be very low at $5.99 \times 10^{-12}$ g/L [47]; no data for gelled $Ce(OH)_4$ appear to be available, which also is the case for $CeO_2{\cdot}2H_2O$. It also is not possible to determine a true solubility of $CeO_2$ owing to the formation of the passivating hydrated surface layer, so the solubility reported for anhydrous $CeO_2$, which is $6.82 \times 10^{-14}$ g/L [48], actually is that of a mixture of a majority of solid $CeO_2{\cdot}2H_2O$ and a minority of gelled $Ce(OH)_4$, as shown in the speciation diagram of Figure 4. Since anhydrous phases typically have solubility product constants

that are greater (by less than an order of magnitude) than the corresponding hydrated phases [49], it then can be assumed that the solubility of pure $CeO_2$, if it could be determined, would be greater than that of both solid $CeO_2 \cdot 2H_2O$ and gelled $Ce(OH)_4$. Hence, the solubility of pure $CeO_2$ probably is greater than that of both of the phases comprising the passivating layer.

The recent experimental investigation of $CeO_2$ solubility in water by Plakhova et al. [48] revealed two relevant phenomena:

- The solubility of $CeO_2$ in basic solutions (pH 7.00–12.00) was independent of the pH. The authors speculated that this suggested that $Ce(OH)_4$ is the predominant solute under these conditions. However, in light of the speciation diagram of Figure 4, this speculation cannot be supported because the dense passivating layer is established rapidly at a pH slightly greater than 2.00, after which no $Ce^{4+}$ or $Ce^{3+}$ species can be dissolved from the underlying $CeO_2$ and only a small amount from the surface $CeO_2 \cdot 2H_2O$.
- No $Ce^{4+}$-based species were generated at a pH in the range 2.00–7.00. Although this was attributed to reductive solubility, these data are consistent with (a) completion of the hydrolysis sequence by a pH of ~2.60, as shown in Figure 4, and (b) commencement of the establishment of the coherent passivating layer from the formation of solid $CeO_2 \cdot 2H_2O$ at a pH slightly greater than 2.00 and gelled $Ce(OH)_4$ at a pH greater than ~2.60, also as shown in Figure 4.

The final point concerning the cerium speciation diagrams is that each valence is treated separately, so it is possible that there are significant $Ce^{4+} \leftrightarrow Ce^{3+}$ equilibria. A relevant question is whether solid $CeO_2 \cdot 2H_2O$ or gelled $Ce(OH)_4$ could react with dissolved $Ce^{3+}$ or $Ce(OH)^{2+}$ to form solid $Ce(OH)_3$ and thus alter the hydrated surface layer. The Gibbs standard free energies of the relevant reactions are highly positive [43], so these reactions are not considered to be likely possibilities.

The calculated Fe speciation diagrams are given in Figures 6 and 7. Figure 6 shows that ferric ($Fe^{3+}$) ions have a pH stability range between that of $Ce^{4+}$ and $Ce^{3+}$, followed by a hydrolysis progression over a wide pH range. Dinuclear $Fe_2(OH)_2{}^{4+}$ forms from $Fe(OH)^{2+}$ and trinuclear $Fe_3(OH)_4{}^{5+}$ forms from $Fe_2(OH)_2{}^{4+} + Fe(OH)^{2+}$ [50,51]. Figure 7 shows that ferrous ($Fe^{2+}$) ions have the largest pH stability range of the four cation species, followed by a relatively narrow pH range for the hydrolysis progression. There are no polynuclear species.

The preceding observations can be considered in terms of two fundamental parameters; the field strength [52], which is the ratio of ionic charge/radius ($Z/r$), and the ionic strength [53], which is one half the summation of the square of the ionic charge times the concentration ($c$) of each species in solution $\left(\frac{1}{2}\Sigma[Z^2c]\right)$. Examination of the Shannon crystal radii for eightfold coordination [16] indicates that the field strengths of $Ce^{4+}$, $Fe^{3+}$, $Ce^{3+}$, and $Fe^{2+}$ are 3.60, 3.26, 2.34, and 1.89, respectively. Figures 4–7 show that the pH stability ranges of these ionic species are inversely proportional to these values, which are a reflection of the electrostatic potentials that attract hydroxyl groups.

Once these species have been hydrolyzed, they can form polynuclear species and the tendency to do this is known to be enhanced by high ionic strengths [44,54]. The examination of Figures 4–7 in terms of the number of species, their valences, and their relative (low) concentrations at the apices of the curves for the polynuclear species suggests that the ionic strengths of $Ce^{4+}$, $Fe^{3+}$, and $Ce^{3+}$ are greater than that of $Fe^{2+}$. The combination of the low field strength of $Fe^{2+}$, which would suppress hydrolysis, and its relatively low ionic strength, when considered in isolation, is considered to be the reason for the observed absence of the associated polynuclear species, although their presence at high species concentrations has been suggested [45].

Finally, the HYDRA database [42] did not include information for dinuclear $Ce_2(OH)_2{}^{4+}$, although it has been reported to exist [45]. If this is the case, then both the $Ce^{3+}$-$H_2O$ and $Fe^{3+}$-$H_2O$ speciation diagrams would indicate the presence of two polynuclear species. The $Ce^{4+}$-$H_2O$ speciation diagram probably indicates a single polynuclear species since valences higher than 6+ are uncommon in dilute solutions. The formation of the polynuclear species of lower valence also probably enhances the potential to form a second polynuclear species of higher valence owing to the associated increase in ionic strength of the solution.

Although the speciation diagrams cover the full range of normal pH (as well as those of extremely high acidity, i.e., at very high species concentrations), the first part of this sequence of publications [8] reported data for the photocatalysis of $CeO_2$ nanoparticles suspended in aqueous solutions in a spiral reactor. Thus, the specific pH of an aqueous suspension of $CeO_2$ was determined by adding 0.1 g of $CeO_2$ nanoparticles to 100 mL of $H_2O$, magnetically stirring the solution, and monitoring the pH until a constant value was attained (which occurred within 48 h). This was found to yield a pH of 7.60. This procedure was repeated for the sample containing the nominal Fe dopant level of 2.00 mol % (1.73 mol % measured) and the variation was minor, yielding a pH of 7.47.

The data in the speciation diagrams for the iron species indicate that the main species that leach from the $Ce_{1-y}Fe_yO_{2-x}$ in water at a pH of 7.60 are $Fe(OH)_3$, $Fe(OH)_2^+$, and $Fe^{2+}$; the other species present at much lower concentrations are $Fe(OH)_4^-$, $Fe(OH)^{2+}$, $Fe(OH)^+$, and $Fe(OH)_2$. However, since iron was present as a dopant only up to a level of 2.00 mol % (1.73 mol % measured) [8] and the initial surface dissolution of the particles occurred only prior to passivation, it can be assumed that the concentrations of the iron species are uniformly negligible.

Table 2 gives the relative concentrations of the ionic species identified in the speciation diagrams at a pH of 7.60. These data represent a starting point in that they indicate the types and concentrations of the species calculated to be present in the solution. While the basic assumptions already have been stated, other factors may be relevant, particularly the influence of localized surface equilibria and whether or not the redox couples are in equilibrium [55,56]. These are clearly key issues owing to the $Ce^{4+}/Ce^{3+}$ and $Fe^{3+}/Fe^{2+}$ redox couples, the potential for intervalence charge transfer effects [57,58], and the effects of these equilibria on the overall and localized redox potential of the solution.

**Table 2.** Calculated relative concentrations of different Ce- and Fe-based species in aqueous solution at a pH of 7.60 in air.

| Parent Ion | Cerium and Iron Species | Relative Concentration (mol %) |
|---|---|---|
| $Ce^{4+}$ | $CeO_2{\cdot}2H_2O$ (*s*) | 69 |
| | $Ce(OH)_4$ (*gel*) | 30 |
| | $Ce(OH)_3^+$ | $<10^{-4}$ |
| $Ce^{3+}$ | $Ce^{3+}$ | 86 |
| | $Ce(OH)^{2+}$ | 13 |
| | $Ce(OH)_2^+$ | 0.3 |
| | $Ce(OH)_3$ | $<10^{-3}$ |
| $Fe^{3+}$ | $Fe(OH)_3$ | 91.5 |
| | $Fe(OH)_2^+$ | 7.5 |
| | $Fe(OH)_4^-$ | <1.0 |
| | $Fe(OH)^{2+}$ | $<10^{-3}$ |
| $Fe^{2+}$ | $Fe^{2+}$ | 99.7 |
| | $Fe(OH)^+$ | <0.1 |
| | $Fe(OH)_2$ | $<10^{-4}$ |

### *2.4. Pourbaix Diagrams*

Pourbaix diagrams use thermodynamic data to extend the approach of speciation diagrams by the simultaneous indication of chemical (as a function of pH) and electrochemical (as a function of electrochemical potential) reactions. They are constructed using three types of straight lines [59,60]:

(1) Vertical lines showing chemical reactions in which no electron transfer occurs; these lines, which bound two predominance regions, correspond to the pH at which both species are of equal concentration (i.e., where the speciation diagram curves intersect).

(2) Horizontal lines showing electrochemical reactions in which no proton transfer occurs; these lines, which also bound two predominance regions, correspond to the standard reduction potentials for the two species.

(3) Diagonal lines showing reactions in which both electron transfer and proton transfer occur; the slopes are inversely proportional to the stoichiometric number of electrons transferred and are directly proportional to the stoichiometric number of protons transferred.

The calculated Ce-$H_2O$ and Fe-$H_2O$ Pourbaix diagrams are given in Figures 8 and 9, respectively. The relevant part of each diagram is the central white region, which defines the conditions for which water is stable. Since there is no applied potential, a line at $E$ = 0 can be considered to define the general equilibria for the full range of possible pH. However, as discussed previously, there will be deviations from this line owing to localized surface equilibria and whether or not the redox couples are in equilibrium [55,56].

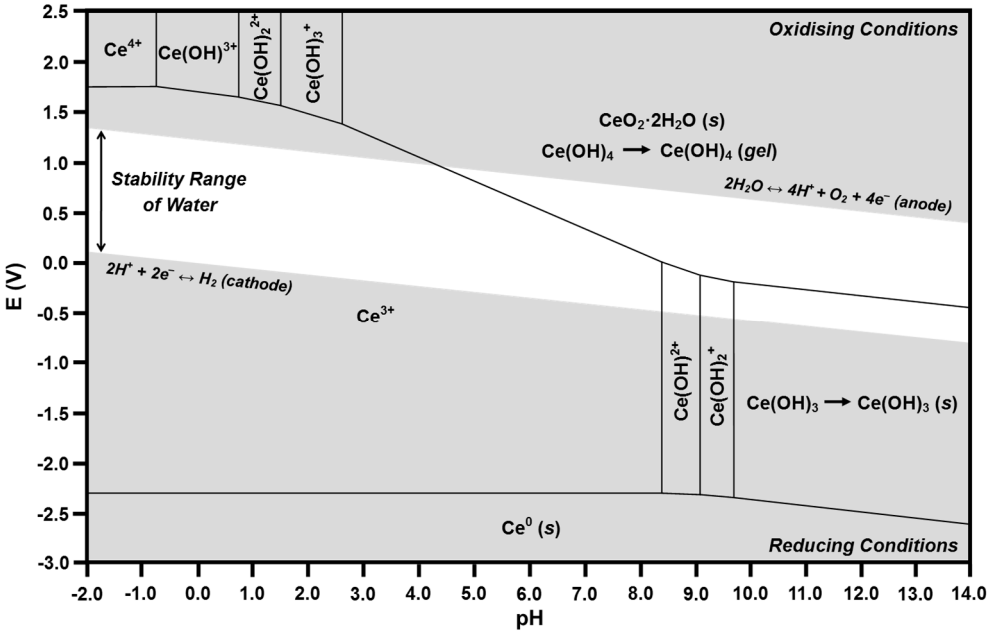


**Figure 8.** Calculated Pourbaix diagram for Ce-$H_2O$.

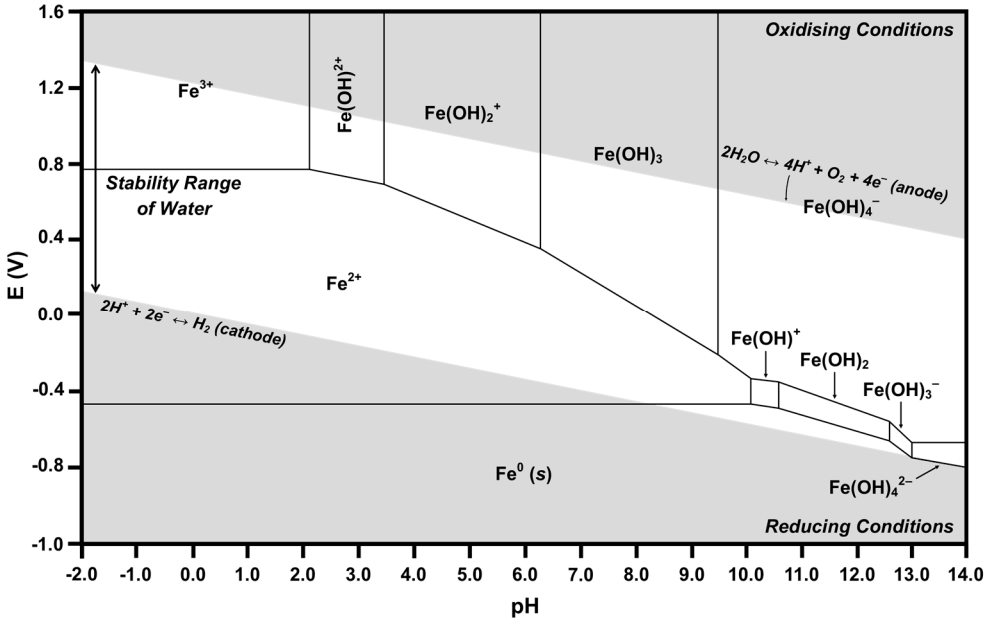


**Figure 9.** Calculated Pourbaix diagram for Fe-$H_2O$.

The method to construct the diagrams involves the use of three equations. The first step requires the calculation of the standard reduction potential ($E^0$) from the Gibbs standard free energy of reaction according to Equation (7) [61]:

$$\Delta G_r^0 = -n\ E^0 \mathrm{F} \quad (7)$$

where:

$\Delta G_r^0$ = Gibbs standard free energy of reaction (J/mol)
$n$ = Stoichiometric number of electrons transferred (valence change)
$E^0$ = Standard reduction potential (V)
F = Faraday constant (96,485 J/V·mol)

The second step is to use the van't Hoff equation (Equation (6) [41]) to determine the applicable pH range and then to apply the Nernst equation (Equation (8) [61]) to determine the electrochemical potential ($E$) for each relevant reaction (assuming the activity coefficients of all species and water to be unity):

$$E = E^0 - \left(\frac{0.0591\ h}{n}\right)\mathrm{pH} + \left(\frac{0.0591}{n}\right)\log\left(\frac{a_{Red}}{a_{Ox}}\right) \quad (8)$$

where:

$E$ = Electrochemical potential (V)
$E^0$ = Standard reduction potential (V)
$h$ = Stoichiometric number of protons transferred
$n$ = Stoichiometric number of electrons transferred (valence change)
$a_{Red}$ = Activity of reductant (concentration calculated from the $K_h$)
$a_{Ox}$ = Activity of oxidant (concentration calculated from the $K_h$)

Tables 3 and 4 list the calculated pH ranges and electrochemical potential ranges corresponding to the reactions involving the species given in the speciation diagrams. The data for the polynuclear species cannot be included because the speciation diagrams, which are defined for dilute solutions, do not show curve intersections between the parent and polynuclear species, so there can be no redox couples. That is, the polynuclear species would be included only if the systems were calculated for very high concentrations.

In the present work, the pH range has been extended to −2.0 in order to show the existence of $Ce^{4+}$ [43]. The calculation of the presence of $Ce^{4+}$ at these unusually low pH values supports the conclusion that the negative pH values are associated with the high concentrations of $Ce^{4+}$ and $Ce^{3+}$ ions at the liquid-solid interface, thereby generating the asymptotic pH gradient discussed previously.

**Table 3.** Electrochemical potentials required for redox reactions ($E$) for Ce species corresponding to speciation diagrams [43,62–65] *.

| No. | Redox Couple Reaction | pH Range | *E* Range |
|---|---|---|---|
| | Reactions between $Ce^0$ and Ce (III) | | |
| 1 | $Ce^{3+} + 3e^- \rightarrow Ce^0$ | −2.0–8.4 | 2.32 (pH independent) |
| 2 | $Ce(OH)^{2+} + H^+ + 3e^- \rightarrow Ce^0 + H_2O$ | 8.4–9.1 | −2.15–0.02 pH |
| 3 | $Ce(OH)_2{}^+ + 2H^+ + 3e^- \rightarrow Ce^0 + 2H_2O$ | 9.1–9.7 | −1.97–0.04 pH |
| 4 | $Ce(OH)_3 + 3H^+ + 3e^- \rightarrow Ce^0 + 3H_2O$ | 9.7–14 | −1.78–0.06 pH |
| | Reactions between $Ce^{3+}$ and Ce (IV) | | |
| 5 | $Ce^{4+} + e^- \rightarrow Ce^{3+}$ | −2.0–−0.76 | 1.74 (pH independent) |
| 6 | $Ce(OH)^{3+} + H^+ + e^- \rightarrow Ce^{3+} + H_2O$ | −0.76–0.72 | 1.69–0.06 pH |
| 7 | $Ce(OH)_2{}^{2+} + 2H^+ + e^- \rightarrow Ce^{3+} + 2H_2O$ | 0.72–1.5 | 1.74–0.12 pH |
| 8 | $Ce(OH)_3{}^+ + 3H^+ + e^- \rightarrow Ce^{3+} + 3H_2O$ | 1.5–2.6 | 1.83–0.18 pH |
| 9 | $Ce(OH)_4 + 4H^+ + e^- \rightarrow Ce^{3+} + 4H_2O$ | 2.6–8.4 | 1.98–0.24 pH |
| | Reactions between Ce (III) and Ce (IV) | | |
| 10 | $Ce(OH)_4 + 3H^+ + e^- \rightarrow Ce(OH)^{2+} + 3H_2O$ | 8.4–9.1 | 1.48–0.18 pH |
| 11 | $Ce(OH)_4 + 2H^+ + e^- \rightarrow Ce(OH)_2{}^+ + 2H_2O$ | 9.1–9.7 | 0.94–0.12 pH |
| 12 | $Ce(OH)_4 + H^+ + e^- \rightarrow Ce(OH)_3 + H_2O$ | 9.7–14 | 0.37–0.06 pH |

* The selected Gibbs standard free energies of reaction generally are from Hayes et al. [43]; when the relevant data were absent, the averages of the most commonly cited values were used.

**Table 4.** Electrochemical potentials required for redox reactions (*E*) for Fe species corresponding to speciation diagrams [54,66–70] *.

| No. | Redox Couple Reaction | pH Range | *E* Range |
|---|---|---|---|
| | Reactions between $Fe^0$ and Fe (II) | | |
| 1 | $Fe^{2+} + 2e^- \rightarrow Fe^0$ | 0–10.1 | −0.47 (pH independent) |
| 2 | $Fe(OH)^+ + H^+ + 2e^- \rightarrow Fe^0 + H_2O$ | 10.1–10.6 | −0.17–0.03 pH |
| 3 | $Fe(OH)_2 + 2H^+ + 2e^- \rightarrow Fe^0 + 2H_2O$ | 10.6–12.6 | 0.09–0.06 pH |
| 4 | $Fe(OH)_3^- + 3H^+ + 2e^- \rightarrow Fe^0 + 3H_2O$ | 12.6–13.0 | 0.50–0.09 pH |
| 5 | $Fe(OH)_4^{2-} + 4H^+ + 2e^- \rightarrow Fe^0 + 4H_2O$ | 13.0–14.0 | 0.89–0.12 pH |
| | Reactions between $Fe^{2+}$ and Fe (III) | | |
| 6 | $Fe^{3+} + e^- \rightarrow Fe^{2+}$ | 0–2.12 | 0.77 (pH independent) |
| 7 | $Fe(OH)^{2+} + H^+ + e^- \rightarrow Fe^{2+} + H_2O$ | 2.12–3.48 | 0.90–0.06 pH |
| 8 | $Fe(OH)_2^+ + 2H^+ + e^- \rightarrow Fe^{2+} + 2H_2O$ | 3.48–6.30 | 1.10–0.12 pH |
| 9 | $Fe(OH)_3 + 3H^+ + e^- \rightarrow Fe^{2+} + 3H_2O$ | 6.30–9.50 | 1.47–0.18 pH |
| 10 | $Fe(OH)_4^- + 4H^+ + e^- \rightarrow Fe^{2+} + 4H_2O$ | 9.50–10.1 | 2.05–0.24 pH |
| | Reactions between Fe (II) and Fe (III) | | |
| 10 | $Fe(OH)_4^- + 3H^+ + e^- \rightarrow Fe(OH)^+ + 3H_2O$ | 10.1–10.6 | 1.46–0.18 pH |
| 11 | $Fe(OH)_4^- + 2H^+ + e^- \rightarrow Fe(OH)_2 + 2H_2O$ | 10.6–12.6 | 0.93–0.12 pH |
| 12 | $Fe(OH)_4^- + H^+ + e^- \rightarrow Fe(OH)_3^- + H_2O$ | 12.6–13.0 | 0.08–0.06 pH |
| 13 | $Fe(OH)_4^- + e^- \rightarrow Fe(OH)_4^{2-}$ | 13.0–14.0 | −0.68 (pH independent) |

* The averages of the most commonly cited values were used.

According to Table 2, the predominant soluble species in the Ce-$H_2O$ system at a pH of 7.60 should be $Ce^{3+}$ and $Ce(OH)^{2+}$, with precipitated $CeO_2 \cdot 2H_2O$ and gelled $Ce(OH)_4$ present as solids. The corresponding Pourbaix diagram shows that the intersection at an *E* of 0 and a pH of 7.60 is located in the $Ce^{3+}$ predominance region. Within the region of water stability, this predominance region bounds those of $Ce(OH)^{2+}$, precipitated $CeO_2 \cdot 2H_2O$ (*s*), and $Ce(OH)_4$ (*gel*). Consequently, these species are in mutual equilibrium. Furthermore, these regions are relatively close to the intersection, so the concentrations of the adjacent species are relatively high. Thus, both speciation diagrams and Pourbaix diagrams reveal the species that are in equilibrium but the former gives absolute concentrations (fixed at a total of 10 μM) and the latter indicates relative concentrations.

The $Ce^{3+}$ predominance region also bounds those for $Ce^{4+}$, $Ce(OH)^{3+}$, $Ce(OH)_2^{2+}$, $Ce(OH)_3^+$, and $Ce^0$ outside of the region of water stability. Examination of Figures 4 and 5 reveals that these species (except $Ce^0$, which is a solid) are given in the speciation diagrams. Although these phenomena may appear to be contradictory, the speciation diagrams and Pourbaix diagrams agree in that both show that, if $Ce^{4+}$ is the starting ion, it rapidly hydrolyzes with increasing pH to form $Ce(OH)^{3+}$, $Ce(OH)_2^{2+}$, and $Ce(OH)_3^+$, finally resulting in the precipitation of $CeO_2 \cdot 2H_2O$ (*s*) and the conversion $Ce(OH)_4$ (*aq*) → $Ce(OH)_4$ (*gel*). In contrast, if the starting ion is $Ce^{3+}$, it remains stable as the pH increases to 7.60. Both diagrams show these phenomena.

The preceding solubility mechanism for $Ce^{4+}$ can considered to be *direct dissolution* in that direct hydrolysis from $Ce^{4+}$ through to the end-products of $CeO_2 \cdot 2H_2O$ (*s*) and $Ce(OH)_4$ (*gel*) takes place as the pH progresses toward 7.60. Although the majority of this path would be required to occur in a region where water is not stable, it is possible because the localized pH and electrochemical potential at the liquid-solid interface, which are unknown, could facilitate this. In Figure 8, this dissolution pathway is *clockwise*.

However, the more thermodynamically probable solubility mechanism is known as *reductive dissolution*, where $Ce^{4+}$ is reduced by water to $Ce^{3+}$ [23–25], which is highly stable as a soluble species, as indicated in the speciation diagram of Figure 5. Although this mechanism is not well known for the Ce-$H_2O$ system, it is well established for the Fe-$H_2O$ [71] and Mn-$H_2O$ [72] systems. The Pourbaix diagram also illustrates the potential for this mechanism, where the $Ce^{4+}$ present on the surface of $CeO_2$ is not in equilibrium with water in the region of water stability, so the $Ce^{4+} \rightarrow Ce^{3+}$ reduction occurs spontaneously, thereby shifting the composition into the $Ce^{3+}$ predominance region, after which it

hydrolyzes to $Ce(OH)^{2+}$ and then to the end-products of $CeO_2 \cdot 2H_2O$ (*s*) and $Ce(OH)_4$ (*gel*) as the pH progresses toward 7.60. $Ce(OH)_2{}^+$ and $Ce(OH)_3$ are not formed because their predominance regions do not bound that of $Ce^{3+}$. In Figure 8, this dissolution pathway is *counterclockwise*.

Many Pourbaix diagrams for the Fe-$H_2O$ system have been calculated for the purpose of examining the corrosion of metallic iron [54,73]. In the present work, Fe at low concentrations is dissolved in the $CeO_2$ lattice in ionic form; therefore, only soluble species, not solids, are considered. For the Fe-$H_2O$ system at a pH of 7.60, Table 2 shows the predominant species as $Fe^{2+}$, $Fe(OH)_2{}^+$, and $Fe(OH)_3$. The intersection at an *E* of 0 and a pH of 7.60 is located in the $Fe^{2+}$ predominance region, which bounds the predominance regions for the full range of pH within the region of water stability of $Fe^{3+}$, $Fe(OH)^{2+}$, $Fe(OH)_2{}^+$, $Fe(OH)_3$, $Fe(OH)_4{}^-$, $Fe(OH)^+$, and $Fe^0$. However, of these, the two predominance regions closest to that of the intersection are those of $Fe(OH)_2{}^+$ and $Fe(OH)_3$. Consequently, the speciation diagram of Figure 6 confirms the predominance of these two species, the speciation diagram of Figure 7 confirms the predominance of $Fe^{2+}$, and all three are confirmed by the Pourbaix diagram of Figure 9. All other species in the three diagrams are present at lower concentrations. Of the latter species, Table 2 reports data for all species except $Fe^{3+}$. The reason for its absence is shown in Figure 6, which demonstrates that the curve is off-scale at a pH of 7.60. $Ce^0$ and $Fe^0$ are not relevant because they are solids.

## 3. Discussion

Consideration of the chemistry and electrochemistry of aqueous systems typically involves the assumption of equilibrium conditions. Consequently, speciation and Pourbaix diagrams, in common with thermodynamic stability diagrams, do not indicate kinetics. The data generated in the present work suggest that a general view of $CeO_2$ and Fe-doped $CeO_2$ requires focusing on the surface of the particles, which effectively are reduced partially owing to the presence of $Ce^{3+}$ and associated oxygen vacancies. The surface layer consists of $CeO_{2-x}$, where x decreases as the oxygen vacancies are filled upon exposure to water, the concept of which is supported by other studies [26,27]. This phenomenon clearly is subject to the consideration of kinetics.

Using $CeO_2 + Ce_2O_3$ and $Fe_2O_3 + FeO$ as reflections of the respective mixed oxidized and reduced conditions of the surface, the general equilibria for the immersion of Fe-doped $CeO_{2-x}$ nanoparticles in water are given in Figure 10.

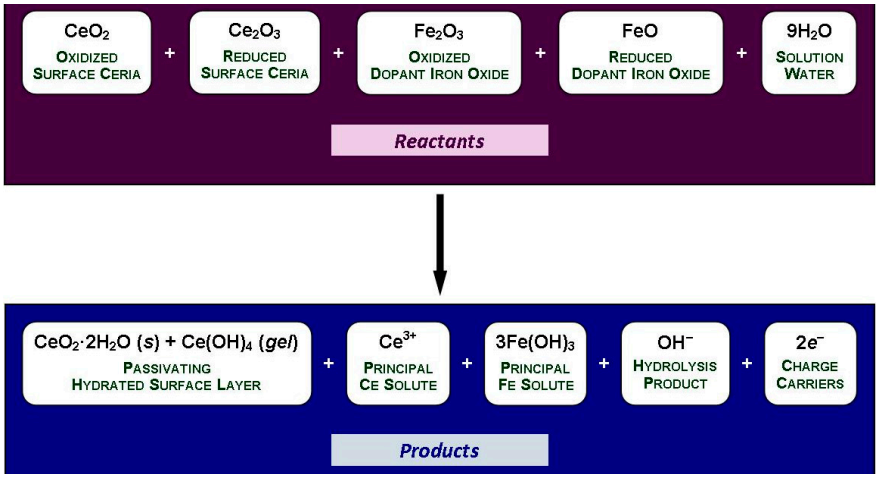


**Figure 10.** General equilibria for the immersion of Fe-doped $CeO_2$ in water.

In reality, equilibrium conditions rarely are met in most situations involving the processing of materials. In these cases, the localized redox equilibria become significant since steady-state conditions are not established during dissolution. That is, the system can be viewed as being in a state of flux owing to localized changes in pH and electrochemical potential. These potentially arise from chemical

gradients resulting from, inter alia, differential redox kinetics, dissolution kinetics, inhomogeneous surface conditions (viz., irregular oxygen vacancy concentrations), solution turbulence, temperature gradients, and differential light exposure of the photocatalyst.

Many of the preceding issues are relevant to investigations of $CeO_2$. The first part of this sequence of publications [8] described work on Fe-doped $CeO_2$ nanopowders to degrade two organic acids in a spiral reactor, which would have established turbulent flow conditions. This would have served to disrupt the boundary layer. However, subsequent work on the same material [74] also reported the retention of photocatalytic activity of thin films of Fe-doped $CeO_2$ in static methyl orange solution. Consequently, the photocatalysis mechanism appears to operate in both turbulent and static flow conditions.

Another potential effect on the redox equilibria is intervalence charge transfer involving the matrix and dopant, which could occur according to Equations (9) and (10) [57,58]:

$$\text{Matrix Only:} \qquad Ce^{4+} + Ce^{4+} \leftrightarrow 2Ce^{3+} + V_O^{\bullet\bullet} \tag{9}$$

$$\text{Matrix and Dopant:} \qquad Ce^{3+} + Fe^{3+} \leftrightarrow Ce^{4+} + Fe^{2+} \tag{10}$$

The present work suggests that the surface layer of $CeO_2$ plays a critical role in the response to immersion in water. That is, as shown in Figure 11, the surface of $CeO_2$ forms a hydrated surface layer of precipitated solid $CeO_2{\cdot}2H_2O$ and gelled $Ce(OH)_4$, which effectively passivates the underlying $CeO_2$. Since it would be expected that any oxygen vacancies associated with the $CeO_2$ component of $CeO_2{\cdot}2H_2O$ would be filled upon precipitation in the aqueous environment by chemisorbed $H_2O$, it can be assumed that there would be little $Ce^{3+}$ initially present in $CeO_2{\cdot}2H_2O$. This effectively would limit the localized equilibria for both of the components of the hydrated surface layer to $Ce^{4+}$-$H_2O$ equilibria, which culminates in the precipitation of solid $CeO_2{\cdot}2H_2O$ and the gelation of $Ce(OH)_4$, as shown in the speciation diagram (Figure 4) and the Pourbaix diagram (Figure 8). The limited redissolution of $CeO_2{\cdot}2H_2O$ during prolonged immersion would increase the proportion of gelled $Ce(OH)_4$ to some extent over time.

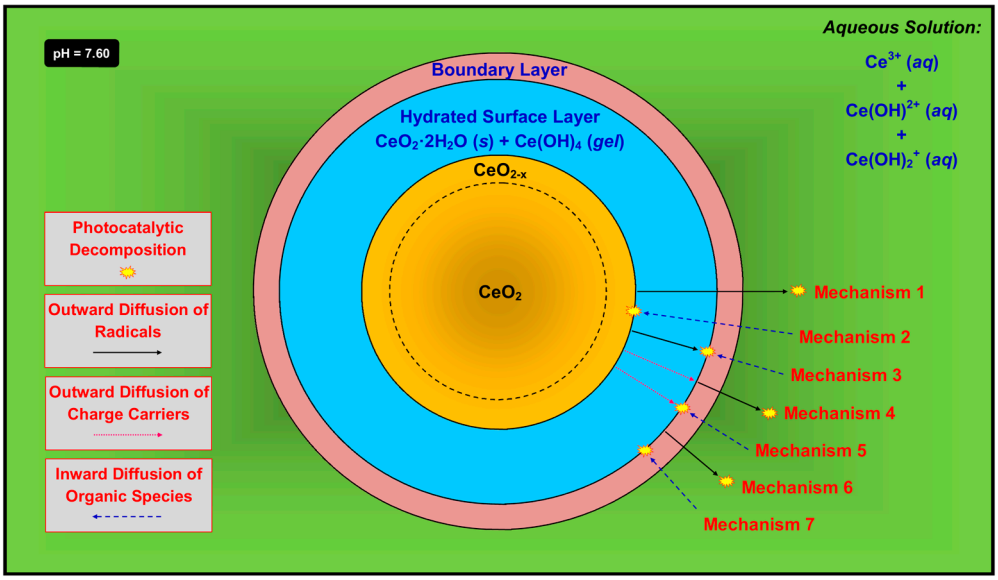


**Figure 11.** Simplified schematic of the potential mechanisms for the activation of $CeO_2$ photocatalyst and the decomposition of organic species.

However, reductive dissolution effectively would introduce the relevant $Ce^{3+}$-$H_2O$ equilibria, again leading to the same hydrated surface layer of precipitated solid $CeO_2{\cdot}2H_2O$ and gelled $Ce(OH)_4$, albeit by a different solubility pathway.

In the environment of the spiral reactor, continuous fluid agitation existed, which would have tended to disrupt the boundary layer and hence to expose the hydrated surface layer. However, under static liquid conditions [74], a saturated boundary layer of species of the same type as leached from the solid would have been established [37–39].

A critical anomaly is the observation of the maintenance of photocatalytic activity in the presence of a hydrated surface layer and possible boundary layer [74]. It would be expected that $CeO_2$ is required for photocatalysis but this phase is passivated and hence not present at the surface. As shown in Figure 11, there are seven possible mechanisms that can explain this effect, where photocatalysis occurs at different locations to form radicals ($\bullet O_2^-$ and $\bullet$OH, both of which have an unpaired electron [$\bullet$]) according to Equations (11) and (12):

$$\text{Oxygen + Electron:} \qquad O_2 + e' \rightarrow \bullet\, O_2^- \tag{11}$$

$$\text{Hydroxyl + Electron Hole:} \qquad OH^- + h^\bullet \rightarrow \bullet OH \tag{12}$$

(1) Mechanism 1—The radicals form at the outer surface of the unhydrated solid, followed by outward diffusion through the hydrated surface layer and boundary layer and into the solution, at which point they decompose the organic species. This is possible but its probability is mitigated by two key factors. First, the radicals, both of which contain an unpaired electron, would have to diffuse through the $Ce(OH)_4$ gel, which is likely to be highly ionic. Second, the radicals also would have to diffuse through the boundary layer, which is comprised largely of positively charged ions in solution. The superoxide radical $\bullet\, O_2^-$ also would tend to be neutralized by the positive ions. However, the concentrations of these species in the boundary layer can be assumed to be quite low, so they may have a minimal effect on the combination of radical and solute.

(2) Mechanism 2—The radicals form at the outer surface of the unhydrated solid and, simultaneously, the organic species undergo inward diffusion through the boundary layer and the hydrated surface layer, followed by reactions to decompose the organic species. This is very unlikely owing to the difficulty of diffusion of what typically are large organic ions not through liquid but the hydrated surface layer, which consists of solid $CeO_2{\cdot}2H_2O$ plus gelled $Ce(OH)_4$ [43].

(3) Mechanism 3—The radicals form at the outer surface of the unhydrated solid, followed by outward diffusion through the hydrated surface layer. In the opposite direction, the organic species undergo inward diffusion through the boundary layer, followed by reactions to decompose the organic species. This is unlikely since each radical, which contains an unpaired electron, would have to diffuse through the highly ionic $Ce(OH)_4$ gel.

(4) Mechanism 4—The charge carriers, which form at the outer surface of the unhydrated solid and/or in the bulk, undergo outward diffusion through the hydrated surface layer, at which point the radicals form. These diffuse through the boundary layer and then into the solution, followed by reactions to decompose the organic species. This is unlikely since the charge carriers would have to diffuse through the highly ionic $Ce(OH)_4$ gel. Furthermore, this is unlikely for electrons because this would require them to diffuse through the boundary layer, which contains positively charged ions in solution. It also is unlikely for holes because this would require them to diffuse through a positively charged environment, which contradicts Le Chatelier's principle [75].

(5) Mechanism 5—The charge carriers, which form at the outer surface of the unhydrated solid and/or in the bulk, undergo outward diffusion through the hydrated surface layer. In the opposite direction, the organic species undergo inward diffusion through the boundary layer, followed by reactions to decompose the organic species. This is unlikely since the charge carriers would have to diffuse through the highly ionic $Ce(OH)_4$ gel.

(6) Mechanism 6—The charge carriers form at the outer surface of the hydrated surface layer or, less likely, in its bulk. The radicals thus form at the outer surface of the hydrated surface layer, followed by their outward diffusion through the boundary layer and into the solution, at which point they decompose the organic species. This is unlikely because the radicals, each of which contains an unpaired electron, must diffuse through the boundary layer, which is comprised largely of positively charged ions in solution, and the superoxide radical $\bullet\, O_2^-$ would tend to be neutralized.

(7) Mechanism 7—The charge carriers form at the outer surface of the hydrated surface layer or, less likely, in its bulk, followed by radical formation. The organic species undergo inward diffusion through the boundary layer, followed by reactions to decompose the organic species. This is possible as this mechanism does not include any of the conceptual shortcomings described previously.

In light of the preceding comments, Mechanism 7 is considered the most probable process for photocatalysis by $CeO_2$ that is immersed in an aqueous solution. If this is correct, an important ramification is that the hydrated surface layer, which consists of a majority of solid $CeO_2 \cdot 2H_2O$ and a minority of gelled $Ce(OH)_4$, is photocatalytic owing to the presence of the precipitated $CeO_2$, even though it is bonded to $H_2O$ molecules. Furthermore, it is probable that these nanoprecipitates, which could be expected to be well dispersed owing to their separation by water molecules, are highly photoactive owing to their highly exposed surface areas (relative to volume). The phenomena of Mechanism 7 are supported by the observation that photocatalysis of Fe-doped $CeO_2$ was observed in both static [74] and turbulent [8] flow conditions.

Furthermore, the nanoprecipitates also probably are considerably smaller than the parent particles (~6 nm). If so, then it is possible that they may be sufficiently small to exhibit the quantum confinement size effect, which could be expected to increase their photocatalytic performance significantly [76–79]. For photocatalytic $TiO_2$, this has been suggested to result in a fourfold increase in performance [76,80–83].

The features of Mechanism 7 are incorporated in a more comprehensive proposed model for photocatalysis, which is shown in Figure 12. Owing to space limitations, the diffusion of the organic species through the boundary layer is not indicated.

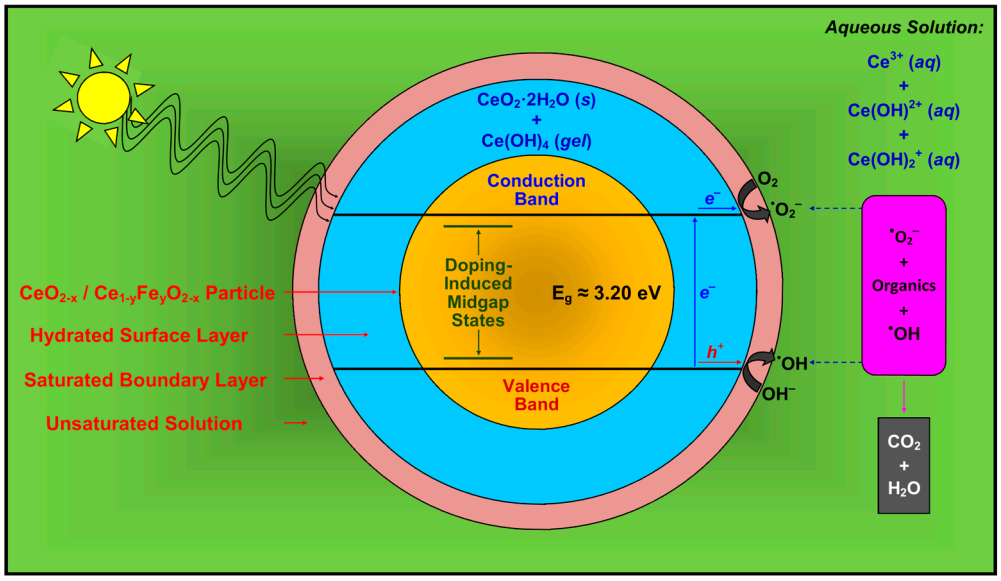


**Figure 12.** Simplified schematic of Mechanism 7 for the activation of $CeO_2$ and Fe-doped $CeO_2$ photocatalyst and the decomposition of organic species, where photocatalysis occurs at the outer surface of the hydrated surface layer of solid $CeO_2 \cdot 2H_2O$ and gelled $Ce(OH)_4$.

Radiation almost certainly would be able to penetrate the thin passivating layer and activate the underlying $CeO_2$. However, since the passivating layer is coherent, then this underlying $CeO_2$ would not contribute to the photocatalysis because it would not be in contact with the surrounding species in solution.

It is reiterated that the exposure of nanoceria to water vapor resulted in weight gains ranging from ~29 wt % for undoped $CeO_2$ to ~34 wt % for $CeO_2$ doped with 2 mol % Fe (1.73 mol % measured). It is difficult to rationalize these large weight gains in terms of just a passivating hydrated surface layer of commensurate thickness. Consequently, it is probable that the hydrated surface layer, which is

expected to be relatively thin, is permeable to water vapor but impermeable to liquid water. That is, $CeO_2$ is hygroscopic and so absorbs water vapor but, paradoxically, the establishment of the coherent, passivating, hydrated surface layer suppresses permeability to liquid water and therefore stabilizes it against further hydration. Consequently, assuming that $Ce^{3+}$ and associated oxygen vacancies are located mainly on the grain surfaces, the *absorption* of water vapor in the *bulk volume* involves initial $Ce^{4+}$-$H_2O$ equilibria and probably subsequent $Ce^{3+}$-$H_2O$ equilibria from the $Ce^{4+} \rightarrow Ce^{3+}$ reduction. In contrast, the *adsorption* of liquid water on the *surface* involves initial $Ce^{4+}$-$H_2O$ equilibria and initial and subsequent $Ce^{3+}$-$H_2O$ equilibria. All of these equilibria would result in the ultimate formation of a majority of solid $CeO_2{\cdot}2H_2O$ and a minority of gelled $Ce(OH)_4$.

During immersion in water, both absorption and adsorption could occur until a continuous layer of gelled $Ce(OH)_4$ effectively passivates the surface. Since some polymers show the dual characteristics of permeability to vapors but impermeability to liquids [84] and these depend on the degree of cross linking, then this suggests the importance of $Ce(OH)_4$ in the hydrated surface layer, which is gelled [43], the condition of which is well known in ceramics [85], Portland cements [86], and geopolymers [87] to involve cross linked hydroxyl groups. In this scenario, gelled $Ce(OH)_4$ would provide passivation and the precipitated $CeO_2{\cdot}2H_2O$ would act as the photocatalyst. It also is possible that a sufficient amount of precipitated $CeO_2{\cdot}2H_2O$ could act as a coherent passivating layer, as in the case of some oxidized metals [88].

Finally, Fe doping caused the photocatalytic performance to increase and this was associated with the apparently contradictory observations of decreasing band gap [8] but increasing hydration (present work). While the former would be expected potentially to increase the photoactivity, the latter would be expected to diminish or eliminate it. The retention of photocatalytic activity in the presence of the hydrated surface layer supports the conclusion of the proposed mechanism. That is, although Fe doping increased the amount of hydration and probably the corresponding volume of the hydrated surface layer, an increase in photocatalytic performance would be expected, provided there is a corresponding increase in the surface distribution density of the nanoprecipitates of $CeO_2$ that are present in $CeO_2{\cdot}2H_2O$.

## 4. Summary and Conclusions

The present work is the second part of a sequence of publications describing the effects of Fe doping on photocatalysis by $CeO_2$ in a spiral reactor. The data demonstrate the critical importance of water exposure because $CeO_2$ is hygroscopic and hence absorbs water vapor but, more importantly, liquid water results in the formation of a hydrated surface layer. While this layer would be expected to eliminate the photoactivity, this did not occur. Calculation of the speciation and Pourbaix diagrams and consideration of the unknown effects of the localized chemical and redox equilibria highlight the critical importance of the establishment of a hydrated surface layer, which consists of a majority of solid $CeO_2{\cdot}2H_2O$ and a minority of gelled $Ce(OH)_4$. A model for the mechanism of photocatalysis by the $CeO_2$ component of the hydrated phase $CeO_2{\cdot}2H_2O$ has been proposed, which explains the observation of the retention of photocatalysis following apparent degradation of the surface of $CeO_2$ upon hydration.

**Acknowledgments:** The support of Naresuan University and the National Research Council of Thailand gratefully are acknowledged. The authors also wish to acknowledge the support of the Materials Science Research Center, Department of Chemistry, Faculty of Science, Chiang Mai University. The authors also are grateful for access to the characterization facilities of the Australian Microscopy & Microanalysis Research Facilities (AMMRF) node at UNSW Sydney.

**Author Contributions:** S.P. and C.C.S. conceived and designed the experiments and analyses; D.C. performed the experiments; D.C., S.S.M., and P.K. undertook the calculations; S.P., A.N., P.K., and C.C.S. analyzed the data; D.C. wrote the initial draft of the paper; C.C.S. wrote the subsequent and final drafts of the paper.

**Conflicts of Interest:** The authors declare no conflict of interest.

## References


1. Channei, D.; Nakaruk, A.; Phanichphant, S.; Koshy, P.; Sorrell, C.C. Cerium Dioxide Thin Films Using Spin Coating. *J. Chem.* **2012**, *2013*, doi:10.1155/2013/579284. [CrossRef]
2. Siriwong, C.; Wetchakun, N.; Inceesungvorn, B.; Channei, D.; Samerjai, T.; Phanichphant, S. Doped-Metal Oxide Nanoparticles for Use as Photocatalysts. *Prog. Cryst. Growth Charact. Mater.* **2012**, *58*, 145–163. [CrossRef]
3. Channei, D.; Inceesungvorn, B.; Wetchakun, N.; Phanichphant, S. Kinetics Study of Photocatalytic Activity of Flame-Made Unloaded and Fe-Loaded $CeO_2$ Nanoparticles. *Int. J. Photoenergy* **2013**, *2013*, doi:10.1155/2013/484831. [CrossRef]
4. Lin, C.Y.W.; Channei, D.; Koshy, P.; Nakaruk, A.; Sorrell, C.C. Effect of Fe Doping on $TiO_2$ Films Prepared by Spin Coating. *Ceram. Int.* **2012**, *38*, 3943–3946. [CrossRef]
5. Leea, J.H.; Euna, J.H.; Parka, S.Y.; Kimb, S.G.; Kima, H.Y. Hydration of RF Magnetron Sputtered MgO Thin Films for a Protective Layer in AC Plasma Display Panel. *Thin Solid Films* **2003**, *435*, 95–101. [CrossRef]
6. Engkvist, O.; Stone, A.J. Adsorption of Water on the MgO (001) Surface. *Surf. Sci.* **1999**, *437*, 239–248. [CrossRef]
7. Zhao, Y. Design of Higher-*k* and More Stable Rare Earth Oxides as Gate Dielectrics for Advanced CMOS Devices. *Materials* **2012**, *5*, 1413–1438. [CrossRef]
8. Channei, D.; Inceesungvorn, B.; Wetchakun, N.; Phanichphant, S.; Nakaruk, A.; Koshy, P.; Sorrell, C.C. Photocatalytic Activity under Visible Light of Fe-doped $CeO_2$ Nanoparticles Synthesized by Flame Spray Pyrolysis. *Ceram. Int.* **2013**, *39*, 3129–3134. [CrossRef]
9. Okamoto, J. Ce-O (Cerium-Oxygen). *J. Phase Equilib. Diffus.* **2008**, *29*, 545–547. [CrossRef]
10. Tuller, H.L.; Nowick, A.S. Defect Structure and Electrical Properties of Nonstoichiometric $CeO_2$ Single Crystals. *J. Electrochem. Soc.* **1979**, *126*, 209–217. [CrossRef]
11. Li, L.; Wang, H.; Zou, L.; Wang, X. Controllable Synthesis, Photocatalytic and Electrocatalytic Properties of $CeO_2$ Nanocrystals. *RSC Adv.* **2015**, *5*, 41506–41512. [CrossRef]
12. Muduli, S.K.; Wang, S.; Chen, S.; Ng, C.F.; Huan, C.H.A.; Sum, T.C.; Soo, H.S. Mesoporous Cerium Oxide Nanospheres for the Visible-Light Driven Photocatalytic Degradation of Dyes. *Beilstein J. Nanotechnol.* **2014**, *5*, 517–523. [CrossRef] [PubMed]
13. Farahani, H.; Wagiran, R.; Hamidon, M.N. Humidity Sensors Principle, Mechanism, and Fabrication Technologies: A Comprehensive Review. *Sensors* **2014**, *14*, 7881–7939. [CrossRef] [PubMed]
14. Kröger, F.A.; Vink, H.J. Relations between the Concentrations of Imperfections in Crystalline Solids. *J. Phys. Chem. Solids* **1958**, *5*, 307–435. [CrossRef]
15. Trovarelli, A. Catalytic Properties of Ceria and $CeO_2$-Containing Materials. *Catal. Rev.* **2006**, *38*, 439–520. [CrossRef]
16. Shannon, R.D. Revised Effective Ionic Radii and Systematic Studies of Interatomic Distances in Halides and Chalcogenides. *Acta Crystallogr. A* **1976**, *32*, 751–767. [CrossRef]
17. Hume-Rothery, W.; Smallman, R.E.; Haworth, C.W. *The Structure of Metals and Alloys*, 5th ed.; Belgrave Square Publications: London, UK, 1969; pp. 349–407.
18. Liao, X.H.; Zhu, J.M.; Zhu, J.J.; Xu, J.Z.; Chen, H.Y. Preparation of Monodispersed Nanocrystalline $CeO_2$ Powders by Microwave Irradiation. *Chem. Commun.* **2001**, *10*, 937–938. [CrossRef]
19. Patterson, A.L. The Scherrer Formula for X-Ray Particle Size Determination. *Phys. Rev.* **1939**, *56*, 978–982. [CrossRef]
20. Fan, L.-S.; Zhu, C. *Principles of Gas-Solid Flows*; Cambridge University Press: Cambridge, UK, 1998; pp. 3–16.
21. Brunauer, S.; Emmett, P.H.; Teller, E. Adsorption of Gases in Multi-Molecular Layers. *J. Am. Chem. Soc.* **1938**, *60*, 309–319. [CrossRef]
22. Haynes, W.M. Physical Constants of Inorganic Compounds. In *CRC Handbook of Chemistry and Physics*, 97th ed.; Lide, D.R., Bruno, T.J., Eds.; CRC Press: Boca Raton, FL, USA, 2017.
23. Beaudoux, X.; Virot, M.; Chave, T.; Leturcq, G.; Jouan, G.; Venault, L.; Moisy, P.; Nikitenko, S.I. Ultrasound-Assisted Reduction Dissolution of $CeO_2$ and $PuO_2$ in the Presence of Ti Particles. *Dalton Trans.* **2016**, *45*, 8802–8815. [CrossRef] [PubMed]
24. Schwabe, F.; Schulin, R.; Rupper, P.; Rotzetter, A.; Stark, W.; Nowack, B. Dissolution and Transformation of Cerium Oxide Nanoparticles in Plant Growth Media. *J. Nanopart. Res.* **2014**, *16*. [CrossRef]

25. Schwabe, F.; Tanner, S.; Schulin, R.; Rotzetter, A.; Stark, W.; von Quadt, A.; Nowack, B. Dissolved Cerium Contributes to Uptake of Ce in the Presence of Differently Sized $CeO_2$-Nanoparticles by Three Crop Plants. *Metallomics* **2015**, *7*, 466–477. [CrossRef] [PubMed]
26. Zhang, C.; Michaelides, A.; King, D.A.; Jenkins, S.J. Anchoring Sites for Initial Au Nucleation on $CeO_2$ {111}: O Vacancy Versus Ce Vacancy. *J. Phys. Chem. C* **2009**, *113*, 6411–6417. [CrossRef]
27. Gritschneder, S.; Reichling, M. Structural Elements of $CeO_2$ (111) Surfaces. *Nanotechnology* **2007**, *18*, 1–6. [CrossRef]
28. Fronzi, M.; Piccinin, S.; Delley, B.; Traversa, E.; Stampfla, C. Water Adsorption on the Stoichiometric and Reduced $CeO_2$ (111) Surface: A First-Principles Investigation. *Phys. Chem. Chem. Phys.* **2009**, *11*, 9188–9199. [CrossRef] [PubMed]
29. Namai, Y.; Fukui, K.; Iwasawa, Y. The Dynamic Behavior of $CH_3OH$ and $NO_2$ Adsorbed on $CeO_2$ (111) Studied by Noncontact Atomic Force Microscopy. *Nanotechnology* **2004**, *15*, 49–54. [CrossRef]
30. Fukui, K.; Namai, Y.; Iwasawa, Y. Imaging of Surface Oxygen Atoms and their Defect Structures on $CeO_2$ (111) by Noncontact Atomic Force Microscopy. *Appl. Surf. Sci.* **2002**, *188*, 252–256. [CrossRef]
31. Gritschneder, S.; Namai, Y.; Iwasawa, Y.; Reichling, M. Structural Features of $CeO_2$ (111) Revealed by Dynamic SFM. *Nanotechnology* **2005**, *16*, 41–48. [CrossRef]
32. Sanchez, M.G.; Gazquez, J.L. Oxygen Vacancy Model in Strong Metal-Support Interaction. *J. Catal.* **1987**, *104*, 120–135. [CrossRef]
33. Pojanavaraphana, C.; Luengnaruemitchaia, A.; Gularic, E. Effect of Support Composition and Metal Loading on Au Catalyst Activity in Steam Reforming of Methanol. *Int. J. Hydrog. Energy* **2012**, *37*, 14072–14084. [CrossRef]
34. Tabakova, T.; Avgouropoulos, G.; Papavasiliou, J.; Manzoli, M.; Boccuzzi, F.; Tenchev, K. CO-Free Hydrogen Production over $Au/CeO_2$–$Fe_2O_3$ Catalysts: Part 1. Impact of the Support Composition on the Performance for the Preferential CO Oxidation Reaction. *Appl. Catal. B Environ.* **2011**, *101*, 256–265. [CrossRef]
35. Bale, C.W.; Chartrand, P.; Degterov, S.A.; Eriksson, G.; Hack, K.; Ben Mahfoud, R.; Melançon, J.; Pelton, A.D.; Petersen, S. FactSage Thermochemical Software and Databases. *Calphad* **2002**, *26*, 189–228. [CrossRef]
36. Birks, N.; Meier, G.H.; Pettit, F.S. *Introduction to the High Temperature Oxidation of Metals*, 2nd ed.; Cambridge University Press: Cambridge, UK, 2006; pp. 83–87.
37. Bingham, P.A.; Connelly, A.J.; Hyatt, N.C.; Hand, R.J. Corrosion of Glass Contact Refractories for the Vitrification of Radioactive Wastes: A Review. *Int. Mater. Rev.* **2013**, *56*, 226–242. [CrossRef]
38. Latreche, H.; Doublet, S.; Schütze, M. Development of Corrosion Assessment Diagrams for High Temperature Chlorine Corrosion. Part I: State of the Art and Development of the Basis for a New Extended Approach. *Oxid. Met.* **2009**, *72*, 1–30. [CrossRef]
39. vanLoon, G.W.; Duffy, S.J. *Environmental Chemistry: A Global Perspective*, 3rd ed.; Oxford University Press: New York, NY, USA, 2011; pp. 227–250.
40. Wilkin, R.T.; Wallschläger, D.; Ford, R.G. Speciation of Arsenic in Sulfidic Waters. *Geochem. Trans.* **2003**, *4*, 1–7. [CrossRef]
41. Doris, K.; Kenneth, E. Chemical Principles Revisited: The Chemistry of Glass. *J. Chem. Educ.* **1979**, *56*, 604–608.
42. KTH/CHE/MEDUSA Downloads. School of Chemical Science and Engineering, KTH Royal Institute of Technology. Available online: https://www.kth.se/en/che/medusa/downloads-1.386254 (accessed on 1 October 2016).
43. Hayes, S.A.; Yu, P.; O'Keefe, T.J.; O'Keefe, M.J.; Stoffer, J.O. The Phase Stability of Cerium Species in Aqueous Systems I. E-pH Diagram for the Ce-$HClO_4$-$H_2O$ System. *J. Electrochem. Soc.* **2002**, *149*, C623–C630. [CrossRef]
44. Kragten, J.; Dencop-Weever, L.G. Hydroxide Complexes of Cerium (III). *Talanta* **1978**, *25*, 147–150. [CrossRef]
45. Baes, C.F., Jr.; Mesmer, R.E. *The Hydrolysis of Cations*; John Wiley & Sons Ltd.: New York, NY, USA, 1976; pp. 130–146 and pp. 226–237.
46. López, J.M.; Gilbank, A.L.; García, T.; Solsona, B.; Agouram, S.; Torrente-Murciano, L. The Prevalence of Surface Oxygen Vacancies over the Mobility of Bulk Oxygen in Nanostructured Ceria for the Total Toluene Oxidation. *Appl. Catal. B* **2015**, *174–175*, 403–412. [CrossRef]
47. Dahle, J.T.; Arai, Y. Environmental Geochemistry of Cerium: Applications and Toxicology of Cerium Oxide Nanoparticles. *Int. J. Environ. Res. Public Health* **2015**, *12*, 1253–1278. [CrossRef] [PubMed]

48. Plakhova, T.V.; Romanchuk, A.Y.; Yakunin, S.N.; Dumas, T.; Demir, S.; Wang, S.; Minasian, S.G.; Shuh, D.K.; Tyliszczak, T.; Shiryaev, A.A.; et al. Solubility of Nanocrystalline Cerium Dioxide: Experimental Data and Thermodynamic Modeling. *J. Phys. Chem. C* **2016**, *120*, 22615–22626. [CrossRef]
49. Haynes, W.M. Solubility Product Constants. In *CRC Handbook of Chemistry and Physics*, 97th ed.; Lide, D.R., Bruno, T.J., Eds.; CRC Press: Boca Raton, FL, USA, 2017; pp. 5-177–5-178.
50. Brown, P.L.; Ekberg, C. *Hydrolysis of Metal Ions*; Wiley-VCH Verlag: Weinheim, Germany, 2016; pp. 601–618.
51. Crichton, R. *Inorganic Biochemistry of Iron Metabolism: From Molecular Mechanisms to Clinical Consequences*, 2nd ed.; Boelaert, J.R., Braun, V., Hantke, K., Eds.; John Wiley & Sons Ltd.: Chichester, UK, 2001; pp. 4–7.
52. Ahrens, L.H. The Use of Ionization Potentials Part 2. Anion Affinity and Geochemistry. *Geochim. Cosmochim. Acta* **1953**, *3*, 1–29. [CrossRef]
53. Lewis, G.N.; Randall, M. The Activity Coefficient of Strong Electrolytes. *J. Am. Chem. Soc.* **1921**, *43*, 1112–1154. [CrossRef]
54. Beverskog, B.; Puigdomenech, I. Revised Pourbaix Diagrams for Iron at 25–300 °C. *Corros. Sci.* **1996**, *38*, 2121–2135. [CrossRef]
55. Liu, X.; Zhou, K.; Wang, L.; Wang, B.; Li, Y. Oxygen Vacancy Clusters Promoting Reducibility and Activity of Ceria Nanorods. *J. Am. Chem. Soc.* **2009**, *131*, 3140–3141. [CrossRef] [PubMed]
56. Tang, Y.; Zhang, H.; Cui, L.; Ouyang, C.; Shi, S.; Tang, W.; Li, H.; Chen, L. Electronic States of Metal (Cu, Ag, Au) Atom on $CeO_2$ (111) Surface: The Role of Local Structural Distortion. *J. Power Sources* **2012**, *197*, 28–37. [CrossRef]
57. Chen, W.F.; Koshy, P.; Huang, Y.; Adabifiroozjaei, E.; Yao, Y.; Sorrell, C.C. Effects of Precipitation, Liquid Formation, and Intervalence Charge Transfer on the Properties and Photocatalytic Performance of Cobalt- or Vanadium-Doped $TiO_2$ Thin Films. *Int. J. Hydrog. Energy* **2016**, *41*, 19025–19056. [CrossRef]
58. Ren, H.; Koshy, P.; Cao, F.; Sorrell, C.C. Multivalence Charge Transfer in Doped and Co-Doped Photocatalytic $TiO_2$. *Inorg. Chem.* **2016**, *55*, 8071–8081. [CrossRef] [PubMed]
59. Verink, E.D., Jr. Procedure for Constructing Pourbaix Diagrams. *J. Educ. Modul. Mater. Sci. Eng.* **1979**, *1*, 535–560.
60. Verink, E.D., Jr. Simplified Procedure for Constructing Pourbaix Diagrams. In *Uhlig's Corrosion Handbook*, 3rd ed.; Revie, R.W., Ed.; John Wiley & Sons Ltd.: Hoboken, NJ, USA, 2011; pp. 93–102.
61. Serguei, N.L. *Introduction to Electrochemical Science and Engineering*; Taylor and Francis Group: Boca Raton, FL, USA, 2015; pp. 100–102.
62. Bilal, B.A.; Müller, E. Thermodynamic Study of $Ce^{4+}/Ce^{3+}$ Redox Reaction in Aqueous Solutions at Elevated Temperatures. *Z. Naturforsch. A* **1992**, *47a*, 974–984.
63. Brookins, D.G. Eh-pH Diagrams for the Rare Earth Elements at 25 °C and one Bar Pressure. *Geochem. J.* **1983**, *17*, 223–229. [CrossRef]
64. Chirkst, D.E.; Lobacheva, O.L.; Berlinskii, I.V. Gibbs Energies of Formation of Hydroxides of Lanthanides and Yttrium. *Russ. J. Phys. Chem. A* **2010**, *84*, 2047–2050. [CrossRef]
65. Yu, P.; Hayes, S.A.; O'Keefe, T.J.; O'Keefe, M.J.; Stoffer, J.O. The Phase Stability of Cerium Species in Aqueous Systems. *J. Electrochem. Soc.* **2006**, *153*, C74–C79. [CrossRef]
66. Ayala-Luis, K.B.; Koch, C.B.; Hansen, H.C.B. The Standard Gibbs Energy of Formation of Fe(II)Fe(III) Hydroxide Sulfate Green Rust. *Clays Clay Miner.* **2008**, *56*, 633–644. [CrossRef]
67. Lemire, R.J.; Berner, U.; Musikas, C.; Palmer, D.A.; Taylor, P.; Tochiyama, O. *Chemical Thermodynamics of Iron, Part 1*; OECD Publications: Paris, France, 2013; pp. 44–50.
68. Hemingway, B.S.; Seal, R.R., II; Chou, I.M. *Thermodynamic Data for Modelling Acid Mine Drainage Problems: Compilation and Estimation of Data for Selected Soluble Iron-Sulfate Minerals*; Open-File Report 02–161; United States Geological Survey: Reston, VA, USA, 2002.
69. Robie, R.A.; Hemingway, B.S.; Fisher, J.R. *Thermodynamic Properties of Minerals and Related Substances at 298.15 K and 1 Bar (105 Pascals) Pressure and at Higher Temperatures*; U.S. Geological Survey Bulletin 1452; U.S. Government Printing Office: Washington, DC, USA, 1978; pp. 12–13.
70. Hem, J.D.; Cropper, W.H. *Survey of Ferrous-Ferric Chemical Equilibria and Redox Potentials*; U.S. Geological Survey Water-Supply Paper 1459-A; U.S. Government Printing Office: Washington, DC, USA, 1962; pp. 3–10.
71. Suter, D.; Banwart, S.; Stumm, W. Dissolution of Hydrous Iron (III) Oxides by Reductive Mechanisms. *Langmuir* **1991**, *7*, 809–813. [CrossRef]

72. Petrunic, B.M.; MacQuarrie, K.T.B.; Al, T.A. Reductive Dissolution of Mn Oxides in River-Recharged Aquifers: A Laboratory Column Study. *J. Hydrol.* **2005**, *301*, 163–181. [CrossRef]
73. Wulfsberg, G. *Inorganic Chemistry*; University Science Books: Mill Valley, CA, USA, 2000; pp. 288–290.
74. Channei, D.; Inceesungvorn, B.; Wetchakun, N.; Ukritnukun, S.; Nattestad, A.; Chen, J.; Phanichphant, S. Photocatalytic Degradation of Methyl Orange by $CeO_2$ and Fe-Doped $CeO_2$ Films under Visible Light Irradiation. *Sci. Rep.* **2015**, *4*, 5757. [CrossRef] [PubMed]
75. Myers, R. *The Basics of Chemistry*; Greenwood Press: Westport, CT, USA, 2003; pp. 149–151.
76. Anpo, M.; Shima, T.; Kodama, S.; Kubokawa, Y. Photocatalytic Hydrogenation of Propyne with Water on Small-Particle Titania: Size Quantization Effects and Reaction Intermediates. *J. Phys. Chem.* **1987**, *91*, 4305–4310. [CrossRef]
77. Jain, P.; Arun, P. Influence of Grain Size on the Band-Gap of Annealed SnS Thin Films. *Thin Solid Films* **2013**, *548*, 241–246. [CrossRef]
78. Khare, A.; Wills, A.W.; Ammerman, L.M.; Norris, D.J.; Aydil, E.S. Size Control and Quantum Confinement in $Cu_2ZnSnS_4$ Nanocrystals. *Chem. Commun.* **2011**, *47*, 11721–11723. [CrossRef] [PubMed]
79. Ren, H.; Koshy, P.; Chen, W.F.; Qi, S.; Sorrell, C.C. Photocatalytic Materials and Technologies for Air Purification. *J. Hazard. Mater.* **2017**, *325*, 340–366. [CrossRef] [PubMed]
80. Ren, H.; Koshy, P.; Wang, J.; Sorrell, C.C. Pure and Mixed Quantum Size Effects in Doped and Co-doped Photocatalytic $TiO_2$. *J. Mater. Sci.* **2017**, in submission.
81. Wang, C.-C.; Zhang, Z.; Ying, J.Y. Photocatalytic Decomposition of Halogenated Organics over Nanocrystalline Titania. *Nanostruct. Mater.* **1997**, *9*, 583–586. [CrossRef]
82. Cho, C.H.; Han, M.H.; Kim, D.H.; Kim, D.K. Morphology Evolution of Anatase $TiO_2$ Nanocrystals under a Hydrothermal Condition (pH = 9.5) and their Ultra-High Photo-Catalytic Activity. *Mater. Chem. Phys.* **2005**, *92*, 104–111. [CrossRef]
83. Zhang, Z.; Wang, C.-C.; Zakaria, R.; Ying, J.Y. Role of Particle Size in Nanocrystalline $TiO_2$-Based Photocatalysts. *J. Phys. Chem. B* **1998**, *102*, 10871–10878. [CrossRef]
84. Träubel, H. *New Materials Permeable to Water Vapor*; Springer: Berlin, Germany, 1999; pp. 133–152.
85. Rahaman, M.N. *Ceramic Processing and Sintering*, 2nd ed.; Marcel Dekker: New York, NY, USA, 2003; pp. 243–323.
86. Thomas, J.J.; Chen, J.J.; Jennings, H.M.; Neumann, D.A. Ca-OH Bonding in the C-S-H Gel Phase of Tricalcium Silicate and White Portland Cement Pastes Measured by Inelastic Neutron Scattering. *Chem. Mater.* **2003**, *15*, 3813–3817. [CrossRef]
87. Provis, J.L.; Bernal, S.A. Geopolymers and Related Alkali-Activated Materials. *Ann. Rev. Mater. Sci.* **2014**, *44*, 299–327. [CrossRef]
88. Kubaschewski, O.; Hopkins, B.E. *Oxidation of Metals and Alloys*, 2nd ed.; Butterworths: London, UK, 1962; pp. 70–142.